Simulating mechanical wave propagation within the framework of phase-field modelling

Xiaoying Liu[a,b,*], Daniel Schneider[a,c], Simon Daubner[a], and Britta Nestler[a,c]

[a] *Institute for Applied Materials (IAM-CMS), Karlsruhe Institute of Technology, Strasse am Forum 7, Karlsruhe, 76131, Germany*
[b] *School of Materials Science and Engineering, Shandong University, Jinan, 250061, PR China*
[c] *Institute of Digital Materials Science (IDM), Karlsruhe University of Applied Sciences, Moltkestrasse 30, Karlsruhe, 76133, Germany*
[*] *Corresponding author*

Abstract

The microstructural evolution in solids is driven by different factors, such as entropy density, the chemical potential and mechanical energy. The mechanical energy density propagates along with the propagation of the mechanical wave, which has a great influence on the rapid solid-state phase transformation, such as the martensitic transformation. In order to determine the mechanical contribution to the driving force during the microstructural evolution, it is therefore indispensable to simulate the mechanical wave propagation within a multiphase and multigrain system. With the introduction of an order parameter for each phase, the phase-field method is an efficient and robust numerical analysis tool, which obviates the complexity of tracking the interfaces among different phases. In this paper, the phase-field method is extended to simulate the mechanical wave propagation by coupling it with the high-order discontinuous Galerkin method. The jump condition at the sharp interface is derived for mechanical waves with strong and weak discontinuities. Based on the jump condition, the interpolation scheme for the stiffness matrix and the density is formulated with order parameters, so as to derive the driving force for the microstructural evolution. Numerical validations are carried out to verify the jump condition, the interpolation scheme and the accuracy and convergence of this simulation scheme.

Keywords: Phase-field method, High-order discontinuous Galerkin method, Mechanical wave propagation, Jump condition

1 Introduction

The macroscopic material properties are determined by the microstructural morphology of the materials[1,2]. In order to gain an insight into the mechanism of material properties, it is thus indispensable to study the material from the microstructural point of view.

In a multiphase system, the microstructural evolution is driven by configurational forces, which are contributed by different factors, such as entropy density, the chemical potential, mechanical energy and others [3,4]. The evolution process was initially described by the moving free boundary problems with a sharp interface, where the interface thickness was equal to zero. Partial differential equations were utilised to describe the physical mechanisms within the single-phase domains, while boundary conditions were imposed on the interfaces [5,6]. The difference of material properties leads to the jump of energy densities across the sharp interfaces. As a result, it is not practical to track the sharp interfaces when the growing geometry of grains/phases is complicated [7]. In the phase-field method, the order parameter ϕ_α represents the volume fraction of the α phase, which varies smoothly but steeply across the diffuse interfaces with finite thickness. The free energy of a multiphase/multigrain system can be expressed by various physical fields, together with the order parameters. Thus, the process of phase transition can be explicitly expressed as the evolution of order parameters, which is formulated by the variational derivation of free energy with respect to the order parameters, according to the free energy minimization. Therefore, with the introduction of order parameters, one of the most important advantages of the phase-field method is that it can successfully obviate the great effort necessary for tracking the interfaces among different phases/grains [8–10]. The phase-field method has been developed into an efficient and robust numerical analysis tool to study the process of microstructural evolution, such as solidification, grain growth, the lithiation of Si electrodes, film growth, as well as precipitation and crack propagation [11–16].

For the modelling of mechanical processes, homogenisation approaches are mostly used in the phase-field community [17]. Levitas and Warren [18] extended the expression for the anisotropic gradient energy by introducing the interface stresses with the help of geometric nonlinearity. Javanbakht and Levitas [19] studied the phase transformation processes under the conditions of high pressure and a large shear. Ma et al. [20] found that the thermomechanical process significantly influences the microstructural evolution of the TiB/Ti matrix composite through the recrystallisation in the beta phase field. However, using homogenisation approaches leads to interfacial excess energy contributions that distort the balance equations at the interfaces [21,16]. Only in the most recent approaches are the mechanical balance equations at the interfaces used to calculate the effective material properties in the transition areas [22–25]. It has been shown that these models fulfil the mechanical jump conditions and represent the configuration forces during phase transformations in multiphase systems with solids [25]. Furthermore, these approaches have already been extended for the mapping of chemo-mechanically coupled phase transformation processes [26,27], as well as plastification mechanisms [28], and allow the modelling of relevant transformation processes in steels in industrial applications [29–31]. With an improved stress and strain formulation prior to and after a crack initiation, Borden et al. [32] broadened the application scope of the phase-field method to the simulation of a crack initiation and propagation in ductile materials.

For the purpose of simulating the rapid solid-state phase transformation, such as the martensitic transformation, it is indispensable to take the dynamic mechanical energy into consideration [33]. To simulate the ultrasonic wave propagation in polycrystalline metal with columnar structures, Nakahata et al. [34] coupled the finite element method (FEM) with the phase-field method. Borden et al. [35] extended the phase-field method from a quasi-static brittle fracture to the dynamic cases. Henry and Levine [36] and Henry [37] studied the dynamic instabilities of fracture with the phase-field model, under different loading conditions. Henry [38] discussed the limitation of the phase-field method in modelling crack propagation with a wedge of high fracture energy. However, regarding the substitution of the sharp interface within the multiphase/multigrain system by the diffuse interface in the phase-field method, a detailed parameter study and convergence analysis are still missing. The parameter study and convergence analysis

should be the fundamental work and should provide guidelines for the further development of the phase-field method, in simulating the microstructural evolution under dynamic mechanical conditions. In this paper, the high-order discontinuous Galerkin method (DGM), which has been successfully applied in the simulation of the propagation of waves [39–42], is coupled with the phase-field method to investigate elastic wave propagation in a polycrystalline structure. Currently, the research scope is limited to the simulation of infinitesimal deformation. Wave propagation with finite deformation will be formulated and studied in the future.

The remaining part of this paper is organised as follows: In Section 2, the numerical methods adopted in this paper, i.e. the phase-field method and the high-order DGM, are briefly introduced to provide the basic evolution formula. Then, considering the mechanical wave with both strong and weak discontinuities, the jump condition at the sharp interface is investigated in Section 3, which is followed by an interpolation scheme for the stiffness matrix and the density at the diffuse interface. In Section 5, several 1D numerical examples are illustrated and analysed to validate the accuracy of the numerical methods presented in Section 2, the jump condition at the sharp interface derived in Section 3 and the efficiency of the interpolation scheme introduced in Section 4. Suggestions regarding the simulation parameters are provided to obtain accurate numerical results. Moreover, two 2D numerical examples with regular and irregular diffuse interfaces are simulated and analysed to verify the application efficiency. In Section 6, conclusions are drawn.

2 Numerical methods

In this paper, the phase-field method is coupled with the high-order DGM to simulate the mechanical wave propagation within the multiphase/multigrain system, which will be briefly introduced in the following parts of this section.

For the symbols and equations in this paper, the following conventions apply: (1) the scalar variables are written as regular uppercase/lowercase letters, (2) the bold lowercase letters represent vectors, (3) the bold uppercase letters denote matrices and (4) for the lowercase Latin subscripts/superscripts in the equations, the index notation and the Einstein summation convention apply, if no further instructions are given.

2.1 Parametrisation of phases in the phase-field method

In a multiphase system, where the total number of phases is defined as N, the free energy $\mathcal{F}$ is calculated as:

$$\mathcal{F} = \int_V \left[f_{se}(\boldsymbol{\phi}, \boldsymbol{\nabla\phi}) + f_d(\boldsymbol{\phi}, \boldsymbol{\varepsilon}, \boldsymbol{v}) + f(...) \right] \mathrm{d}V \tag{1}$$

where the N-tuple $\boldsymbol{\phi} = (\phi_1, \phi_2, ..., \phi_N)$, and ϕ_α $(\alpha = 1, 2, ..., N)$ is the order parameter for the α phase. The N-tuple $\boldsymbol{\nabla\phi} = (\nabla\phi_1, \nabla\phi_2, ..., \nabla\phi_N)$ contains the gradients of each element in the N-tuple $\boldsymbol{\phi}$, and ∇ is the gradient operator. $f_{se}(\boldsymbol{\phi}, \boldsymbol{\nabla\phi})$ denotes the grain boundary contributions, dependent on the order parameters and their gradients [28,23]. V is the volume of the concerned domain, and $f_d(\boldsymbol{\phi}, \boldsymbol{\varepsilon}, \boldsymbol{v})$ represents the dynamic mechanical energy density derived according to the N-tuple $\boldsymbol{\phi}$, the infinitesimal elastic strain matrix $\boldsymbol{\varepsilon}$ and the material particle velocity vector $\boldsymbol{v}$. $f(...)$ denotes the additional energy densities contributed by factors such as heat, the chemical potential and/or others.

In this paper, only the dynamic mechanical contribution $f_d(\boldsymbol{\phi}, \boldsymbol{\varepsilon}, \boldsymbol{v})$ with infinitesimal elastic strain is considered and derived in detail. The dynamic mechanical contribution with finite strain will be formulated and analysed in future research work. It is worth mentioning that in this paper, the reference configuration is used for geometrical

computing, since infinitesimal elastic strain is under consideration. For the situation with finite strain, the calculation based on the reference configuration will be retained through the combination with the Piola-Kirchhoff stress [24].

In the phase-field method, the order parameter $\phi_\alpha(\boldsymbol{x}, t)$ is used to parametrise the α phase, which physically represents its volume fraction at the location $\boldsymbol{x} = (x_1, x_2, x_3)^T$ and the time t, with $(x_1, x_2, x_3)^T$ defining the material particle position in the Cartesian coordinate system, constructed by the base unit vectors $\{\boldsymbol{e}_1, \boldsymbol{e}_2, \boldsymbol{e}_3\}$. Therefore, the order parameters satisfy the following constraint:

$$\sum_{\alpha=1}^{N} \phi_\alpha(\boldsymbol{x}, t) = 1 \qquad (0 \leq \phi_\alpha(\boldsymbol{x}, t) \leq 1) \tag{2}$$

With order parameters, the parametrisation of a multiphase system can be visually demonstrated as Figure 1. Specifically, $\phi_\alpha = 1$ in the regions with a single α phase, and $\phi_\alpha = 0$ within the grains containing a single β ($\alpha \neq \beta$) phase. Between the phases α and β, there is an interface with finite thickness. In contrast to systems with sharp interfaces, where the volume fraction of a phase is either 1 or 0, the order parameters are diffused and change continuously across the finite-thickness interfaces in the phase-field method, as illustrated on the right side of Figure 1. Here, Eq. (2) is always satisfied in the whole simulation domain.

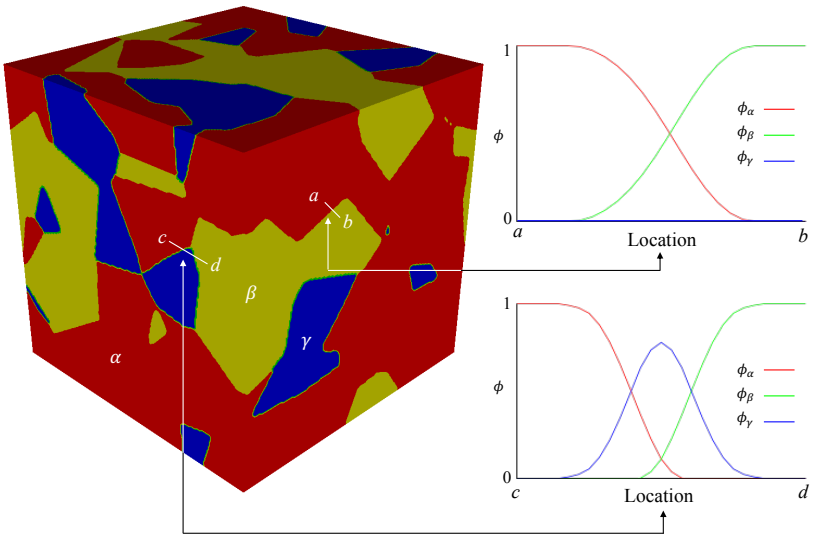

Figure 1: A volume fraction in a multiphase system

With order parameters, the dynamic mechanical energy density $f_d(\boldsymbol{\phi}, \boldsymbol{\varepsilon}, \boldsymbol{v})$ is calculated as the interpolation of phase-dependent contributions:

$$f_d(\boldsymbol{\phi}, \boldsymbol{\varepsilon}, \boldsymbol{v}) = \sum_{\alpha=1}^{N} f_d^\alpha(\boldsymbol{\varepsilon}^\alpha, \boldsymbol{v}^\alpha) h^\alpha(\boldsymbol{\phi}) \tag{3}$$

where $f_d^\alpha(\boldsymbol{\varepsilon}^\alpha, \boldsymbol{v}^\alpha)$ is the dynamic mechanical energy density of the α phase, and $h^\alpha(\boldsymbol{\phi})$ is an interpolation function determined by $\boldsymbol{\phi}$ and constructed with the purpose of interpolating the dynamic mechanical energy density $f_d^\alpha(\boldsymbol{\varepsilon}^\alpha, \boldsymbol{v}^\alpha)$ across the diffuse interfaces. Similar to the order parameter ϕ_α, $h^\alpha(\boldsymbol{\phi})$ satisfies [24]:

$$\sum_{\alpha=1}^{N} h^\alpha(\boldsymbol{\phi}) = 1 \qquad (0 \leq h^\alpha(\boldsymbol{\phi}) \leq 1) \tag{4}$$

With diffused volume fractions and energy densities, the process of the phase transition can be explicitly described by the evolution of the order parameters as follows [43]:

$$\dot{\phi}_\alpha(\boldsymbol{x},t) = -\frac{1}{N}\sum_{\beta=1,\beta\neq\alpha}^{N} M_{\alpha\beta}\left(\frac{\delta\mathcal{F}}{\delta\phi_\alpha} - \frac{\delta\mathcal{F}}{\delta\phi_\beta}\right) \tag{5}$$

where $\dot{\phi}_\alpha(\boldsymbol{x},t) = \partial\phi_\alpha(\boldsymbol{x},t)/\partial t$ is the first-order time derivation of the order parameter ϕ_α, $M_{\alpha\beta}$ represents the mobility for the $\alpha-\beta$ interface [44] and the operator $\delta/\delta\phi_\alpha$ is expressed as:

$$\frac{\delta}{\delta\phi_\alpha} = \frac{\partial}{\partial\phi_\alpha} - \nabla\cdot\frac{\partial}{\partial\nabla\phi_\alpha} \tag{6}$$

where $\nabla\cdot$ denotes the divergence operator.

2.2 High-order DGM

The DGM has been proven to be an efficient numerical tool in simulating wave propagation [39–42]. In this paper, the high-order formulation of DGM is therefore embedded into the phase-field method to study the influence of mechanical wave propagation upon the process of phase transformation. According to Leveque [45], the local governing equations for mechanical wave propagation can be expressed as:

$$\dot{u}_i(\boldsymbol{x},t) = C_{ij}^k u_{j,k}(\boldsymbol{x},t) + s_i(\boldsymbol{x},t) \tag{7}$$

where $u_i(\boldsymbol{x},t)$ $(i=1,2,...,9)$ represents the i-th element in the vector $\boldsymbol{u} = (\sigma_{11},\sigma_{22},\sigma_{33},\sigma_{23},\sigma_{13},\sigma_{12},v_1,v_2,v_3)^T$. The first six elements in $\boldsymbol{u}$ are the Cauchy stress variables in the Voigt notation, while the last three elements are the velocity variables. The subscripts $\{1,2,3\}$ of the elements in $\boldsymbol{u}$ denote the directions $\{\boldsymbol{e}_1,\boldsymbol{e}_2,\boldsymbol{e}_3\}$, respectively; $u_{j,k}(\boldsymbol{x},t)$ is the first-order derivation of $u_j(\boldsymbol{x},t)$ with respect to x_k $(k=1,2,3)$. $s_i(\boldsymbol{x},t)$ denotes the source term corresponding to $u_i(\boldsymbol{x},t)$, C_{ij}^k represents the element in the i-th row and the j-th column of the matrix $\boldsymbol{C}^k$, and $\boldsymbol{C}^k$ is the coefficient matrix which defines the relationship between $\dot{u}_i(\boldsymbol{x},t)$ and $u_{j,k}(\boldsymbol{x},t)$. In this paper, the simulated material is supposed to be isotropic within a single-phase domain. Thus, the matrix $\boldsymbol{C}^k$ is expressed as:

$$
\boldsymbol{C}^1 = \begin{pmatrix}
0 & 0 & 0 & 0 & 0 & 0 & K_{11} & 0 & 0 \\
0 & 0 & 0 & 0 & 0 & 0 & K_{21} & 0 & 0 \\
0 & 0 & 0 & 0 & 0 & 0 & K_{31} & 0 & 0 \\
0 & 0 & 0 & 0 & 0 & 0 & 0 & 0 & 0 \\
0 & 0 & 0 & 0 & 0 & 0 & 0 & 0 & K_{55} \\
0 & 0 & 0 & 0 & 0 & 0 & 0 & K_{66} & 0 \\
\mathcal{R} & 0 & 0 & 0 & 0 & 0 & 0 & 0 & 0 \\
0 & 0 & 0 & 0 & 0 & \mathcal{R} & 0 & 0 & 0 \\
0 & 0 & 0 & 0 & \mathcal{R} & 0 & 0 & 0 & 0
\end{pmatrix}
$$

$$
\boldsymbol{C}^2 = \begin{pmatrix}
0 & 0 & 0 & 0 & 0 & 0 & 0 & K_{12} & 0 \\
0 & 0 & 0 & 0 & 0 & 0 & 0 & K_{22} & 0 \\
0 & 0 & 0 & 0 & 0 & 0 & 0 & K_{32} & 0 \\
0 & 0 & 0 & 0 & 0 & 0 & 0 & 0 & K_{44} \\
0 & 0 & 0 & 0 & 0 & 0 & 0 & 0 & 0 \\
0 & 0 & 0 & 0 & 0 & 0 & K_{66} & 0 & 0 \\
0 & 0 & 0 & 0 & 0 & \mathcal{R} & 0 & 0 & 0 \\
0 & \mathcal{R} & 0 & 0 & 0 & 0 & 0 & 0 & 0 \\
0 & 0 & 0 & \mathcal{R} & 0 & 0 & 0 & 0 & 0
\end{pmatrix}
\tag{8}
$$

$$
\boldsymbol{C}^3 = \begin{pmatrix}
0 & 0 & 0 & 0 & 0 & 0 & 0 & 0 & K_{13} \\
0 & 0 & 0 & 0 & 0 & 0 & 0 & 0 & K_{23} \\
0 & 0 & 0 & 0 & 0 & 0 & 0 & 0 & K_{33} \\
0 & 0 & 0 & 0 & 0 & 0 & 0 & K_{44} & 0 \\
0 & 0 & 0 & 0 & 0 & 0 & K_{55} & 0 & 0 \\
0 & 0 & 0 & 0 & 0 & 0 & 0 & 0 & 0 \\
0 & 0 & 0 & 0 & \mathcal{R} & 0 & 0 & 0 & 0 \\
0 & 0 & 0 & \mathcal{R} & 0 & 0 & 0 & 0 & 0 \\
0 & 0 & \mathcal{R} & 0 & 0 & 0 & 0 & 0 & 0
\end{pmatrix}
$$

where K_{ij} $(i, j = 1, 2, ..., 6)$ forms the effective stiffness matrix $\boldsymbol{K}$, which defines the relationship between the elastic stresses and strains in the Voigt notation:

$$
\boldsymbol{K} = \begin{pmatrix}
K_{11} & K_{12} & K_{13} & 0 & 0 & 0 \\
K_{21} & K_{22} & K_{23} & 0 & 0 & 0 \\
K_{31} & K_{32} & K_{33} & 0 & 0 & 0 \\
0 & 0 & 0 & K_{44} & 0 & 0 \\
0 & 0 & 0 & 0 & K_{55} & 0 \\
0 & 0 & 0 & 0 & 0 & K_{66}
\end{pmatrix}
\tag{9}
$$

In Eq. (8), the reciprocal of the effective density $\mathcal{R}$ is determined by the densities of the simulated materials. As introduced in Section 2.1, the sharp interfaces among the different phases/grains are substituted by diffuse interfaces in the phase-field method, and the order parameter ϕ_α represents the volume fraction of the α phase. In Eq. (8), the material property parameters, i.e. the effective stiffness matrix $\boldsymbol{K}$ and the reciprocal of the effective density $\mathcal{R}$, thus are given in the interpolated form. This means they are formulated by the Lamé parameters λ and μ, the density ρ and the order parameter ϕ_α, which will be derived in detail in Sections 3 and 4.

It can be observed that the first six equations in the series of Eq. (7) are actually the dynamic constitutive equations with stress-velocity formulations, while the last three are the dynamic governing equations expressed by velocity and stress. Since velocity is the first-order derivation of displacement with respect to time t, Eq. (7) is exactly equivalent to the traditional constitutive equations and governing equations with the displacement-stress expression.

In this paper, the high-order DGM is embedded into the multifunctional numerical analysis software PACE3D (Parallel Algorithms for Crystal Evolution in 3D)[1] [46]. In this software, the simulated domain is discretised with an equidistant grid, as illustrated in Figure 2.

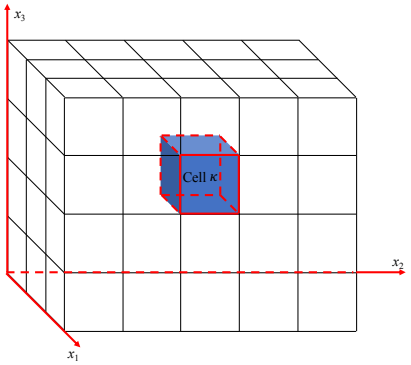

Figure 2: Spatial discretisation in PACE3D

Each cell κ is assigned with a variable vector $\boldsymbol{u}^\kappa$, and its element $u_i^\kappa(\boldsymbol{x},t)$ is spatially approximated by a linear combination of a series of orthogonal polynomials. This results in the following:

$$u_i^\kappa(\boldsymbol{x},t) = a_{ij}^\kappa(t) p_j(\boldsymbol{x}) \tag{10}$$

where $a_{ij}^\kappa(t)$ represents the unknowns for $u_i^\kappa(\boldsymbol{x},t)$ at time t. The orthogonal polynomial basis $p_j(\boldsymbol{x})$ forms the spatially approximating space $\boldsymbol{p} = (p_j(\boldsymbol{x}),\ j = 1, 2, ..., n)$, which satisfies the following requirement:

$$\int_{V_\kappa} p_{j_1}(\boldsymbol{x}) p_{j_2}(\boldsymbol{x})\,\mathrm{d}V_\kappa = \begin{cases} 1 & (j_1 = j_2) \\ 0 & (j_1 \neq j_2) \end{cases} \tag{11}$$

where V_κ is the volume for the cell κ. With the highest polynomial degree equal to q, the number of bases in space $\boldsymbol{p}$, i.e. n, is calculated as:

$$n = \frac{(q+1)(q+2)(q+3)}{6} \tag{12}$$

For the source term $s_i^\kappa(\boldsymbol{x},t)$ within the cell κ, it is also approximated through a linear combination of the bases in $\boldsymbol{p}$, which results in:

$$s_i^\kappa(\boldsymbol{x},t) = b_{ij}^\kappa(t) p_j(\boldsymbol{x}) \tag{13}$$

where $b_{ij}^\kappa(t)$ is calculated according to the Taylor series of the input source function.

For the cell κ, the weak form of Eq. (7) can be written as:

$$\int_{V_\kappa} \dot{u}_i^\kappa(\boldsymbol{x},t) p_l(\boldsymbol{x})\,\mathrm{d}V_\kappa = C_{ij}^{\kappa k} \int_{V_\kappa} u_{j,k}^\kappa(\boldsymbol{x},t) p_l(\boldsymbol{x})\,\mathrm{d}V_\kappa + \int_{V_\kappa} s_i^\kappa(\boldsymbol{x},t) p_l(\boldsymbol{x})\,\mathrm{d}V_\kappa \tag{14}$$

Eq. (14) shows that the elements in the coefficient matrix $\boldsymbol{C}^{\kappa k}$ are considered as constants within the cell κ. According to the product rule of the derivation and the divergence theorem, the first term on the right-hand side of Eq. (14) can be expressed as:

[1] PACE3D is developed by the research group of Prof. Dr. rer. nat. Britta Nestler, at the Karlsruhe Institute of Technology and the Karlsruhe University of Applied Sciences.

$$C_{ij}^{\kappa k}\int_{V_\kappa} u_{j,k}^{\kappa}(\boldsymbol{x},t)p_l(\boldsymbol{x})\,\mathrm{d}V_\kappa = C_{ij}^{\kappa k}\int_{S_\kappa} u_j^{\kappa}(\boldsymbol{x},t)p_l(\boldsymbol{x})\xi_k\,\mathrm{d}S_\kappa - C_{ij}^{\kappa k}\int_{V_\kappa} u_j^{\kappa}(\boldsymbol{x},t)p_{l,k}(\boldsymbol{x})\,\mathrm{d}V_\kappa \tag{15}$$

where S_κ denotes the surface of the cell κ, and $\boldsymbol{\xi} = (\xi_1, \xi_2, \xi_3)^T$ is the outward unit normal vector of the surface S_κ. In order to calculate the interaction or the numerical flux between adjacent cells, the Riemann solver is used with an upwind scheme [39]. Therefore, the first term on the right-hand side of Eq. (15) can be written as:

$$C_{ij}^{\kappa k}\int_{S_\kappa} u_j^{\kappa}(\boldsymbol{x},t)p_l(\boldsymbol{x})\xi_k\,\mathrm{d}S_\kappa = \frac{1}{2}\int_{S_\kappa} T_{ij}^{S_\kappa}(C_{jm}^{\kappa 1} - D_{jm}^{\kappa 1})T_{mr}^{'S_\kappa} u_r^{\kappa}(\boldsymbol{x},t)p_l(\boldsymbol{x})\,\mathrm{d}S_\kappa + \frac{1}{2}\int_{S_\kappa} T_{ij}^{S_\kappa}(C_{jm}^{\kappa 1} + D_{jm}^{\kappa 1})T_{mr}^{'S_\kappa} u_r^{\kappa_{S_\kappa}}(\boldsymbol{x},t)p_l(\boldsymbol{x})\,\mathrm{d}S_\kappa \tag{16}$$

where the symbol κ_{S_κ} in $u_r^{\kappa_{S_\kappa}}(\boldsymbol{x},t)$ refers to the cell which shares the surface S_κ with the cell κ. $\boldsymbol{T}^{S_\kappa}$ represents the matrix transforming the local variables $\boldsymbol{u}^{S_\kappa}$ to the global variables $\boldsymbol{u}^{\kappa}$, i.e. $u_i^{\kappa} = T_{ij}^{S_\kappa} u_j^{S_\kappa}$. With the base unit vectors $\{\boldsymbol{\xi}, \boldsymbol{\eta}, \boldsymbol{\zeta}\} = \{(\xi_1, \xi_2, \xi_3)^T, (\eta_1, \eta_2, \eta_3)^T, (\zeta_1, \zeta_2, \zeta_3)^T\}$ constructing the local Cartesian coordinate system, $\boldsymbol{T}^{S_\kappa}$ is expressed as follows:

$$\boldsymbol{T}^{S_\kappa} = \begin{pmatrix} \xi_1\xi_1 & \eta_1\eta_1 & \zeta_1\zeta_1 & 2\eta_1\zeta_1 & 2\xi_1\zeta_1 & 2\xi_1\eta_1 & 0 & 0 & 0 \\ \xi_2\xi_2 & \eta_2\eta_2 & \zeta_2\zeta_2 & 2\eta_2\zeta_2 & 2\xi_2\zeta_2 & 2\xi_2\eta_2 & 0 & 0 & 0 \\ \xi_3\xi_3 & \eta_3\eta_3 & \zeta_3\zeta_3 & 2\eta_3\zeta_3 & 2\xi_3\zeta_3 & 2\xi_3\eta_3 & 0 & 0 & 0 \\ \xi_2\xi_3 & \eta_2\eta_3 & \zeta_2\zeta_3 & \eta_2\zeta_3 + \eta_3\zeta_2 & \xi_2\zeta_3 + \xi_3\zeta_2 & \xi_2\eta_3 + \xi_3\eta_2 & 0 & 0 & 0 \\ \xi_1\xi_3 & \eta_1\eta_3 & \zeta_1\zeta_3 & \eta_1\zeta_3 + \eta_3\zeta_1 & \xi_1\zeta_3 + \xi_3\zeta_1 & \xi_1\eta_3 + \xi_3\eta_1 & 0 & 0 & 0 \\ \xi_1\xi_2 & \eta_1\eta_2 & \zeta_1\zeta_2 & \eta_1\zeta_2 + \eta_2\zeta_1 & \xi_1\zeta_2 + \xi_2\zeta_1 & \xi_1\eta_2 + \xi_2\eta_1 & 0 & 0 & 0 \\ 0 & 0 & 0 & 0 & 0 & 0 & \xi_1 & \eta_1 & \zeta_1 \\ 0 & 0 & 0 & 0 & 0 & 0 & \xi_2 & \eta_2 & \zeta_2 \\ 0 & 0 & 0 & 0 & 0 & 0 & \xi_3 & \eta_3 & \zeta_3 \end{pmatrix} \tag{17}$$

$\boldsymbol{T}^{'S_\kappa}$ denotes the inverse matrix of $\boldsymbol{T}^{S_\kappa}$. The matrix $\boldsymbol{D}^{\kappa k}$ is determined by the eigenvalues and right eigenvectors of the matrix $\boldsymbol{C}^{\kappa k}$:

$$D_{ij}^{\kappa k} = G_{il}^{\kappa k} H_{lm}^{\kappa k} G_{mj}^{'\kappa k} \tag{18}$$

where the Einstein summation convention does not apply to the superscript k. $\boldsymbol{H}^{\kappa k} = diag(|h_1|, |h_2|, ..., |h_9|)$, where $|h_i|$ $(i = 1, 2, ..., 9)$ is the absolute value of the i-th eigenvalue of the matrix $\boldsymbol{C}^{\kappa k}$ and satisfies the following:

$$h_{i_1} \le h_{i_2} \qquad (i_1 < i_2) \tag{19}$$

The matrix $\boldsymbol{G}^{\kappa k} = (\boldsymbol{g}_1, \boldsymbol{g}_2, ..., \boldsymbol{g}_9)$, with the column vector $\boldsymbol{g}_i$ $(i = 1, 2, ..., 9)$ being the eigenvector of the matrix $\boldsymbol{C}^{\kappa k}$ corresponding to the eigenvalue h_i. In Eq. (16), it is worth noticing that the following equation remains valid when $\boldsymbol{\xi} = \boldsymbol{e}_k$:

$$C_{ij}^{\kappa k} - D_{ij}^{\kappa k} = T_{il}^{S_\kappa}(C_{lm}^{\kappa 1} - D_{lm}^{\kappa 1})T_{mj}^{'S_\kappa} \tag{20}$$

By substituting Eqs. (15) and (16) into Eq. (14), the following formula can be obtained:

$$\begin{aligned}\int_{V_\kappa} \dot{u}_i^\kappa(\boldsymbol{x},t)p_l(\boldsymbol{x})\,\mathrm{d}V_\kappa =& \frac{1}{2}\int_{S_\kappa} T_{ij}^{S_\kappa}(C_{jm}^{\kappa k}-D_{jm}^{\kappa k})T_{mr}^{'S_\kappa}u_r^\kappa(\boldsymbol{x},t)p_l(\boldsymbol{x})\,\mathrm{d}S_\kappa + \\ & \frac{1}{2}\int_{S_\kappa} T_{ij}^{S_\kappa}(C_{jm}^{\kappa k}+D_{jm}^{\kappa k})T_{mr}^{'S_\kappa}u_r^{c_{S_\kappa}}(\boldsymbol{x},t)p_l(\boldsymbol{x})\,\mathrm{d}S_\kappa - \\ & C_{ij}^{\kappa k}\int_{V_\kappa} u_j^\kappa(\boldsymbol{x},t)p_{l,k}(\boldsymbol{x})\,\mathrm{d}V_\kappa + \int_{V_\kappa} s_i^\kappa(\boldsymbol{x},t)p_l(\boldsymbol{x})\,\mathrm{d}V_\kappa\end{aligned} \tag{21}$$

According to Eqs. (10), (11) and (13), as well as the forward finite difference approximation, Eq. (21) can be written as:

$$\begin{aligned}a_{il}^\kappa(t+\Delta t) =& a_{il}^\kappa(t)+\Delta t\left(\frac{1}{2}\int_{S_\kappa} T_{ij}^{S_\kappa}(C_{jm}^{\kappa k}-D_{jm}^{\kappa k})T_{mr}^{'S_\kappa}a_{rs}^\kappa(t)p_s(\boldsymbol{x})p_l(\boldsymbol{x})\,\mathrm{d}S_\kappa + \right. \\ & \frac{1}{2}\int_{S_\kappa} T_{ij}^{S_\kappa}(C_{jm}^{\kappa k}+D_{jm}^{\kappa k})T_{mr}^{'S_\kappa}a_{rs}^{\kappa_{S_\kappa}}(t)p_s(\boldsymbol{x})p_l(\boldsymbol{x})\,\mathrm{d}S_\kappa - \\ & \left. C_{ij}^{\kappa k}\int_{V_\kappa} a_{jm}^\kappa(t)p_m(\boldsymbol{x})p_{l,k}(\boldsymbol{x})\,\mathrm{d}V_\kappa + b_{il}^\kappa(t)\right)\end{aligned} \tag{22}$$

where Δt denotes the timestep for the temporal discretisation.

In this paper, three different boundary conditions are considered, namely free, nonreflective and de-dimension boundary conditions. The first two adapt the formula in Käser and Dumbser[39]. Supposing that the surface S_ι is a free boundary, the numerical flux in Eq. (16) for the surface S_ι is calculated as:

$$\begin{aligned}C_{ij}^{\kappa k}\int_{S_\iota} u_j^\kappa(\boldsymbol{x},t)p_l(\boldsymbol{x})\xi_k\,\mathrm{d}S_\iota =& \frac{1}{2}\int_{S_\iota} T_{ij}^{S_\iota}(C_{jm}^{\kappa 1}-D_{jm}^{\kappa 1})T_{mr}^{'S_\iota}u_r^\kappa(\boldsymbol{x},t)p_l(\boldsymbol{x})\,\mathrm{d}S_\iota + \\ & \frac{1}{2}\int_{S_\iota} T_{ij}^{S_\iota}(C_{jm}^{\kappa 1}+D_{jm}^{\kappa 1})\mathcal{N}_{mr}T_{rs}^{'S_\iota}u_s^{\kappa_{S_\iota}}(\boldsymbol{x},t)p_l(\boldsymbol{x})\,\mathrm{d}S_\iota\end{aligned} \tag{23}$$

where $\boldsymbol{\mathcal{N}} = diag(-1,1,1,1,-1,-1,1,1,1)$. If the surface S_ι is a nonreflective boundary, Eq. (23) becomes:

$$C_{ij}^{\kappa k}\int_{S_\iota} u_j^\kappa(\boldsymbol{x},t)p_l(\boldsymbol{x})\xi_k\,\mathrm{d}S_\iota = \frac{1}{2}\int_{S_\iota} T_{ij}^{S_\iota}(C_{jm}^{\kappa 1}-D_{jm}^{\kappa 1})T_{mr}^{'S_\iota}u_r^\kappa(\boldsymbol{x},t)p_l(\boldsymbol{x})\,\mathrm{d}S_\iota \tag{24}$$

It is noticed that Eq. (23) sets the inward and outward flux as opposite values, for the stress elements which are supposed to be zero at the free boundary. While Eq. (24) fixes the inward flux at the noneflective boundary as zero. As for the de-dimension boundary, it is introduced when investigating some phenomena with 1D or 2D numerical examples on the 3D software platform, i.e. PACE3D. At this time, the inward flux is exactly the same as the outward flux. Thus, assuming that the surface S_ι is a de-dimension boundary, Eq. (23) becomes:

$$\begin{aligned}C_{ij}^{\kappa k}\int_{S_\iota} u_j^\kappa(\boldsymbol{x},t)p_l(\boldsymbol{x})\xi_k\,\mathrm{d}S_\iota =& \frac{1}{2}\int_{S_\iota} T_{ij}^{S_\iota}(C_{jm}^{\kappa 1}-D_{jm}^{\kappa 1})T_{mr}^{'S_\iota}u_r^\kappa(\boldsymbol{x},t)p_l(\boldsymbol{x})\,\mathrm{d}S_\iota + \\ & \frac{1}{2}\int_{S_\iota} T_{ij}^{S_\iota}(C_{jm}^{\kappa 1}+D_{jm}^{\kappa 1})T_{mr}^{'S_\iota}u_r^\kappa(\boldsymbol{x},t)p_l(\boldsymbol{x})\,\mathrm{d}S_\iota \\ =& \int_{S_\iota} T_{ij}^{S_\iota}C_{jm}^{\kappa 1}T_{mr}^{'S_\iota}u_r^\kappa(\boldsymbol{x},t)p_l(\boldsymbol{x})\,\mathrm{d}S_\iota\end{aligned} \tag{25}$$

3 Jump condition at the sharp interface

In this section, the jump condition at the sharp interface between two different phases is investigated, on the basis of which the interpolation of the material parameters within the corresponding diffuse interface can be derived in the phase-field method. For the interface generated by more than two phases, the jump condition and the interpolation scheme presented in this paper can be extended, similar to the method proposed by Schneider et al. [25].

The geometrical description of the physical domain is given as in Figure 3. Ω_α denotes the open domain with a single α phase, which means that $\Omega_\alpha \cap \Gamma_\alpha = \emptyset$, if Γ_α represents the boundary of Ω_α. $\Lambda_{\alpha\beta} = \Gamma_\alpha \cap \Gamma_\beta \setminus \mathcal{P}_{\alpha\beta}$ represents the open domain shared by the boundaries of the α and β phases, i.e. the sharp interface between these phases, and $\mathcal{P}_{\alpha\beta}$ is the boundary of $\Lambda_{\alpha\beta}$. $\Omega_{\alpha\beta} = \Omega_\alpha \cup \Omega_\beta \cup \Lambda_{\alpha\beta}$ denotes the open domain including the α and β phases, and $\Gamma_{\alpha\beta} = \Gamma_\alpha \cup \Gamma_\beta \setminus \Lambda_{\alpha\beta}$ represents the boundary of $\Omega_{\alpha\beta}$.

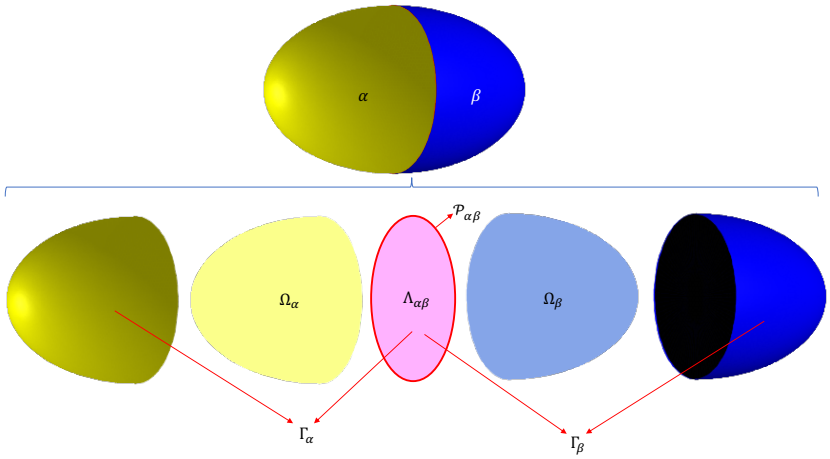

Figure 3: Geometrical description of the physical domain

In order to study the jump condition at the interface $\Lambda_{\alpha\beta}$, it is split into two symmetric parts, Λ_α^β and Λ_β^α, as demonstrated in Figure 4. The coordinate variable $\boldsymbol{x}$ has identical values at the symmetric points, which are respectively located at the surfaces Λ_α^β and Λ_β^α. However, the material properties at the surface Λ_α^β take the values from the α phase, while the material properties at the surface Λ_β^α assume the values from the β phase. Thus, in the domain $\overline{\Omega}_\alpha = \Omega_\alpha \cup \Lambda_\alpha^\beta$, only the α phase is present. The jump of an arbitrary variable $z(\boldsymbol{x}, t)$, at the interface $\Lambda_{\alpha\beta}$, is defined as:

$$[\![z(\boldsymbol{x}, t)]\!]^{\Lambda_{\alpha\beta}} = z^{\Lambda_\alpha^\beta}(\boldsymbol{x}, t) - z^{\Lambda_\beta^\alpha}(\boldsymbol{x}, t) \tag{26}$$

where $z^{\Lambda_\alpha^\beta}(\boldsymbol{x}, t)$ denotes the z field at the surface Λ_α^β.

For the elastic wave propagation within continua, the displacement fields $\boldsymbol{w} = (w_1, w_2, w_3)^T$ of material particles are continuous within the whole simulated domain Ω, according to the continuity condition. In this paper, two different elastic wave types are studied, i.e. elastic waves with strong and weak discontinuities [47]. The definition of the elastic wave with strong discontinuity is given as:

Definition 1. $\forall \varepsilon > 0, \exists \delta_i > 0, \forall \boldsymbol{x} \in \Omega : \|\boldsymbol{x} - \boldsymbol{x}_0\|_2 < \delta_i \implies |w_i(\boldsymbol{x}, t) - w_i(\boldsymbol{x}_0, t)| < \varepsilon$ $(i = 1, 2, 3;\ \boldsymbol{x}_0 \in \Omega;\ t > 0)$.

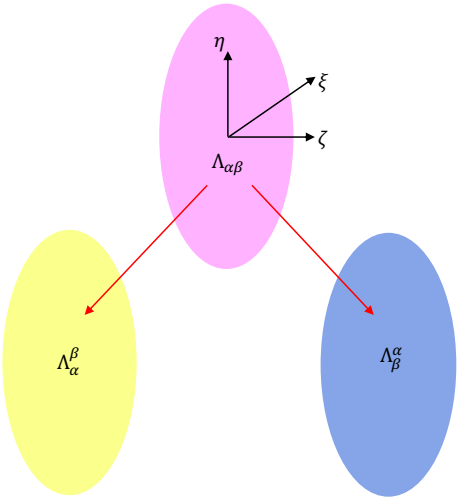

Figure 4: Splitting the interface $\Lambda_{\alpha\beta}$ into Λ_{α}^{β} and Λ_{β}^{α}

On the basis of Definition 1 and with further constraints, the elastic wave with weak discontinuity is defined as follows:

Definition 2. $\forall \varepsilon > 0, \exists \delta_{1ij}, \delta_{2i} > 0$:

(1) $\forall \boldsymbol{x} \in \overline{\Omega}_\alpha, \|\boldsymbol{x} - \boldsymbol{x}_0\|_2 < \delta_{1ij} \implies \left| \frac{\partial w_i(\boldsymbol{x},t)}{\partial x_j} - \frac{\partial w_i(\boldsymbol{x},t)}{\partial x_j}\Big|_{\boldsymbol{x}=\boldsymbol{x}_0} \right| < \varepsilon,$

(2) $\forall t > 0, |t - t_0| < \delta_{2i} \implies \left| \frac{\partial w_i(\boldsymbol{x},t)}{\partial t} - \frac{\partial w_i(\boldsymbol{x},t)}{\partial t}\Big|_{t=t_0} \right| < \varepsilon,\ (i,j = 1,2,3;\ \boldsymbol{x}, \boldsymbol{x}_0 \in \overline{\Omega}_\alpha,\ t, t_0 > 0).$

Here, $\|\cdot\|_2$ refers to the Euclidean norm, which calculates the length of a vector. Definition 1 ensures the continuity of the displacement fields $\boldsymbol{w}$ over the whole domain Ω, while Definition 2 shows that both the first-order spatial and temporal derivations of the displacement fields are continuous within a single-phase domain $\overline{\Omega}_\alpha$. This means that the waveforms of the strains, stresses and velocities are continuous within a single-phase domain $\overline{\Omega}_\alpha$. For brevity, the elastic wave with strong discontinuity is referred to as Type I wave in this paper, while the elastic wave with weak discontinuity is described as Type II wave. Figure 5 respectively illustrates an example for Type I and Type II waves, which are used for numerical analysis in this paper.

The base unit vectors $(\boldsymbol{\xi}, \boldsymbol{\eta}, \boldsymbol{\zeta})^T$ construct the local Cartesian coordinate system at the interface $\Lambda_{\alpha\beta}$, with $\boldsymbol{\xi}$ normal to the interface $\Lambda_{\alpha\beta}$, as shown in Figure 4. Hence, the local stresses and strains can be expressed as follows:

$$\begin{cases} \widetilde{\boldsymbol{\sigma}} &= (\widetilde{\boldsymbol{\sigma}}^1, \widetilde{\boldsymbol{\sigma}}^2)^T = \boldsymbol{M}_\sigma \boldsymbol{\sigma} \\ \widetilde{\boldsymbol{\varepsilon}} &= (\widetilde{\boldsymbol{\varepsilon}}^1, \widetilde{\boldsymbol{\varepsilon}}^2)^T = \boldsymbol{M}_\varepsilon \boldsymbol{\varepsilon} \end{cases} \tag{27}$$

where $\widetilde{\boldsymbol{\sigma}}^1 = (\sigma_{\xi\xi}, \sigma_{\xi\zeta}, \sigma_{\xi\eta})^T$ and $\widetilde{\boldsymbol{\sigma}}^2 = (\sigma_{\eta\eta}, \sigma_{\zeta\zeta}, \sigma_{\eta\zeta})^T$ respectively represent the normal and tangential components in the local stress vector, while $\widetilde{\boldsymbol{\varepsilon}}^1 = (\varepsilon_{\xi\xi}, \varepsilon_{\xi\zeta}, \varepsilon_{\xi\eta})^T$ and $\widetilde{\boldsymbol{\varepsilon}}^2 = (\varepsilon_{\eta\eta}, \varepsilon_{\zeta\zeta}, \varepsilon_{\eta\zeta})^T$ denote the corresponding normal and tangential components in the local strain vector. $\boldsymbol{\sigma}$ and $\boldsymbol{\varepsilon}$ are the global stress and strain fields in the Voigt notation. The local base unit vectors $(\boldsymbol{\xi}, \boldsymbol{\eta}, \boldsymbol{\zeta})^T$ define the transformation matrices $\boldsymbol{M}_\sigma$ and $\boldsymbol{M}_\varepsilon$ as follows:

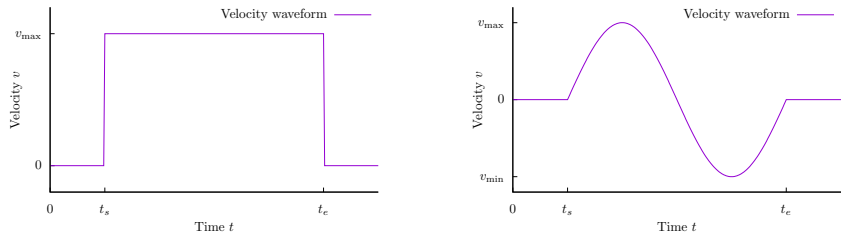

(a) An example of a velocity waveform for a Type I wave

(b) An example of a velocity waveform for a Type II wave

Figure 5: The examples for the Type I and Type II waves (t_s and t_e respectively represent the beginning and the end of the incident wave)

$$
\begin{aligned}
\boldsymbol{M}_\sigma &= \begin{pmatrix}
\xi_1\xi_1 & \xi_2\xi_2 & \xi_3\xi_3 & 2\xi_2\xi_3 & 2\xi_1\xi_3 & 2\xi_1\xi_2 \\
\xi_1\zeta_1 & \xi_2\zeta_2 & \xi_3\zeta_3 & \xi_2\zeta_3+\xi_3\zeta_2 & \xi_1\zeta_3+\xi_3\zeta_1 & \xi_1\zeta_2+\xi_2\zeta_1 \\
\xi_1\eta_1 & \xi_2\eta_2 & \xi_3\eta_3 & \xi_2\eta_3+\xi_3\eta_2 & \xi_1\eta_3+\xi_3\eta_1 & \xi_1\eta_2+\xi_2\eta_1 \\
\eta_1\eta_1 & \eta_2\eta_2 & \eta_3\eta_3 & 2\eta_2\eta_3 & 2\eta_1\eta_3 & 2\eta_1\eta_2 \\
\zeta_1\zeta_1 & \zeta_2\zeta_2 & \zeta_3\zeta_3 & 2\zeta_2\zeta_3 & 2\zeta_1\zeta_3 & 2\zeta_1\zeta_2 \\
\eta_1\zeta_1 & \eta_2\zeta_2 & \eta_3\zeta_3 & \eta_2\zeta_3+\eta_3\zeta_2 & \eta_1\zeta_3+\eta_3\zeta_1 & \eta_1\zeta_2+\eta_2\zeta_1
\end{pmatrix} \\
\boldsymbol{M}_\varepsilon &= \begin{pmatrix}
\xi_1\xi_1 & \xi_2\xi_2 & \xi_3\xi_3 & \xi_2\xi_3 & \xi_1\xi_3 & \xi_1\xi_2 \\
2\xi_1\zeta_1 & 2\xi_2\zeta_2 & 2\xi_3\zeta_3 & \xi_2\zeta_3+\xi_3\zeta_2 & \xi_1\zeta_3+\xi_3\zeta_1 & \xi_1\zeta_2+\xi_2\zeta_1 \\
2\xi_1\eta_1 & 2\xi_2\eta_2 & 2\xi_3\eta_3 & \xi_2\eta_3+\xi_3\eta_2 & \xi_1\eta_3+\xi_3\eta_1 & \xi_1\eta_2+\xi_2\eta_1 \\
\eta_1\eta_1 & \eta_2\eta_2 & \eta_3\eta_3 & \eta_2\eta_3 & \eta_1\eta_3 & \eta_1\eta_2 \\
\zeta_1\zeta_1 & \zeta_2\zeta_2 & \zeta_3\zeta_3 & \zeta_2\zeta_3 & \zeta_1\zeta_3 & \zeta_1\zeta_2 \\
2\eta_1\zeta_1 & 2\eta_2\zeta_2 & 2\eta_3\zeta_3 & \eta_2\zeta_3+\eta_3\zeta_2 & \eta_1\zeta_3+\eta_3\zeta_1 & \eta_1\zeta_2+\eta_2\zeta_1
\end{pmatrix}
\end{aligned}
\tag{28}
$$

where $\boldsymbol{\xi} = (\xi_1, \xi_2, \xi_3)^T$, $\boldsymbol{\eta} = (\eta_1, \eta_2, \eta_3)^T$ and $\boldsymbol{\zeta} = (\zeta_1, \zeta_2, \zeta_3)^T$. It can be seen that $\boldsymbol{M}_\sigma^{'} = \boldsymbol{M}_\varepsilon^T$ and $\boldsymbol{M}_\varepsilon^{'} = \boldsymbol{M}_\sigma^T$.

Similar to the static mechanics [48,23] for both elastic wave types, i.e. Type I and Type II waves, the following equilibrium equations hold true at the interface $\Lambda_{\alpha\beta}$:

$$w_i^{\Lambda_\alpha^\beta}(\boldsymbol{x}, t) = w_i^{\Lambda_\beta^\alpha}(\boldsymbol{x}, t) \tag{29a}$$

$$(\widetilde{\sigma}_i^1)^{\Lambda_\alpha^\beta}(\boldsymbol{x}, t) = (\widetilde{\sigma}_i^1)^{\Lambda_\beta^\alpha}(\boldsymbol{x}, t) \tag{29b}$$

$$(\widetilde{\varepsilon}_i^2)^{\Lambda_\alpha^\beta}(\boldsymbol{x}, t) = (\widetilde{\varepsilon}_i^2)^{\Lambda_\beta^\alpha}(\boldsymbol{x}, t) \tag{29c}$$

$$v_i^{\Lambda_\alpha^\beta}(\boldsymbol{x}, t) = v_i^{\Lambda_\beta^\alpha}(\boldsymbol{x}, t) \tag{29d}$$

where the subscript $i = 1, 2, 3$ denotes the i-th element in the corresponding vector. Eqs. (29a) and (29b) are automatically satisfied, according to the requirements of the material continuity and the force balance at the interface $\Lambda_{\alpha\beta}$. Then, based on Eq. (29a), the following conclusions can be drawn:

$$\frac{\partial w_i^{\Lambda_\alpha^\beta}(\boldsymbol{x},t)}{\partial \widetilde{x}_2} = \frac{\partial w_i^{\Lambda_\beta^\alpha}(\boldsymbol{x},t)}{\widetilde{x}_2} \tag{30a}$$

$$\frac{\partial w_i^{\Lambda_\alpha^\beta}(\boldsymbol{x},t)}{\partial \widetilde{x}_3} = \frac{\partial w_i^{\Lambda_\beta^\alpha}(\boldsymbol{x},t)}{\widetilde{x}_3} \tag{30b}$$

$$\frac{\partial w_i^{\Lambda_\alpha^\beta}(\boldsymbol{x},t)}{\partial t} = \frac{\partial w_i^{\Lambda_\beta^\alpha}(\boldsymbol{x},t)}{\partial t} \tag{30c}$$

where $\widetilde{\boldsymbol{x}} = (\widetilde{x}_1, \widetilde{x}_2, \widetilde{x}_3)^T = \boldsymbol{Q}\boldsymbol{x}$ denotes the material particle position in the local Cartesian coordinate system, and the transformation matrix $\boldsymbol{Q}$ is expressed as:

$$Q = \begin{pmatrix} \xi_1 & \xi_2 & \xi_3 \\ \eta_1 & \eta_2 & \eta_3 \\ \zeta_1 & \zeta_2 & \zeta_3 \end{pmatrix} \tag{31}$$

Thus, Eq. (29c) can be obtained through Eqs. (30a) and (30b), while Eq. (29d) can be obtained through Eq. (30c).

According to Eqs. (26) and (29), the jump condition at the interface $\Lambda_{\alpha\beta}$ can be described as:

$$[\![\boldsymbol{w}(\boldsymbol{x},t)]\!]^{\Lambda_{\alpha\beta}} = 0 \tag{32a}$$

$$[\![\widetilde{\boldsymbol{\sigma}}^1(\boldsymbol{x},t)]\!]^{\Lambda_{\alpha\beta}} = 0 \tag{32b}$$

$$[\![\widetilde{\boldsymbol{\varepsilon}}^2(\boldsymbol{x},t)]\!]^{\Lambda_{\alpha\beta}} = 0 \tag{32c}$$

$$[\![\boldsymbol{v}(\boldsymbol{x},t)]\!]^{\Lambda_{\alpha\beta}} = 0 \tag{32d}$$

At the interface $\Lambda_{\alpha\beta}$, the jump of other mechanical fields, i.e. strains $\widetilde{\boldsymbol{\varepsilon}}^1$, stresses $\widetilde{\boldsymbol{\sigma}}^2$ and momentums $\boldsymbol{\psi} = \rho\boldsymbol{v}$, is determined by the jump of the stiffness matrix and the density.

Through Definitions 1 and 2, it can be observed that the displacement fields $\boldsymbol{w}$ for both Type I and Type II waves are continuous within the whole simulated domain, which can also be ensured by the continuous requirement of continua mechanics. However, it is worth pointing out that the following proposition is only true for the Type II wave:

Proposition 1. $\forall \varepsilon > 0, \exists \delta_{1i}, \delta_{2i}, \delta_{3i} > 0, \forall \boldsymbol{x} \in \Omega_{\alpha\beta}$:

(1) $\|\boldsymbol{x} - \boldsymbol{x}_0\|_2 < \delta_{1i} \implies |\widetilde{\sigma}_i^1(\boldsymbol{x},t) - \widetilde{\sigma}_i^1(\boldsymbol{x}_0,t)| < \varepsilon,$

(2) $\|\boldsymbol{x} - \boldsymbol{x}_0\|_2 < \delta_{2i} \implies |\widetilde{\varepsilon}_i^2(\boldsymbol{x},t) - \widetilde{\varepsilon}_i^2(\boldsymbol{x}_0,t)| < \varepsilon,$

(3) $\|\boldsymbol{x} - \boldsymbol{x}_0\|_2 < \delta_{3i} \implies |v_i(\boldsymbol{x},t) - v_i(\boldsymbol{x}_0,t)| < \varepsilon,\ (i = 1,2,3;\ \boldsymbol{x}_0 \in \Lambda_{\alpha\beta};\ t > 0).$

Proposition 1 states the continuity of the stress fields $\widetilde{\boldsymbol{\sigma}}^1$, strain fields $\widetilde{\boldsymbol{\varepsilon}}^2$ and velocity fields $\boldsymbol{v}$ across the interface $\Lambda_{\alpha\beta}$. For the Type II wave, Proposition 1 can be proven straightforwardly, according to Definition 2 and Eqs. (29b), (29c) and (29d). While the continuity stated by Proposition 1 cannot be ensured for the Type I wave, due to the discontinuity of the first-order spatial or temporal derivation of the displacement fields $\boldsymbol{w}$ within a single-phase domain $\overline{\Omega}_\alpha$, although Eqs. (29b), (29c) and (29d) hold true.

4 Interpolation of material parameters

In order to obviate the effort necessary for tracking interfaces, the sharp interface $\Lambda_{\alpha\beta}$, between the α and β phases, is approximated in PACE3D through a diffuse interface with the order parameter ϕ_α^κ, which represents the volume fraction of the α phase in the cell κ. Therefore, the material stiffness matrix $\overline{\boldsymbol{K}}$ and the density ρ can be interpolated with the order parameters $\boldsymbol{\phi}$, which form the effective stiffness matrix $\boldsymbol{K}$ and the reciprocal of the effective density $\mathcal{R}$ in Eq. (8). This interpolation leads to a diffusion of the jump of the strains $\widetilde{\boldsymbol{\varepsilon}}^1$, stresses $\widetilde{\boldsymbol{\sigma}}^2$ and momentums $\boldsymbol{\psi} = \rho\boldsymbol{v}$ at the interface $\Lambda_{\alpha\beta}$, as well as the dynamic mechanical energy density $f_d(\boldsymbol{\phi}, \boldsymbol{\varepsilon}, \boldsymbol{v})$, since:

$$f_d(\boldsymbol{\phi}, \boldsymbol{\varepsilon}, \boldsymbol{v}) = f_\varepsilon(\boldsymbol{\phi}, \boldsymbol{\varepsilon}) + f_v(\boldsymbol{\phi}, \boldsymbol{v}) \tag{33}$$

where $f_\varepsilon(\boldsymbol{\phi}, \boldsymbol{\varepsilon})$ and $f_v(\boldsymbol{\phi}, \boldsymbol{v})$ are the elastic strain energy density and the kinetic energy density, respectively.

4.1 Interpolation of the stiffness matrix

According to Eqs. (32b) and (32c), it can be concluded that during the mechanical wave propagation, the jump condition for the elastic stresses and strains at the interface $\Lambda_{\alpha\beta}$ is exactly the same as for the static case [23]. Therefore, the interpolation scheme for the effective stiffness matrix $\boldsymbol{K}$, proposed by Schneider et al. [23], is adopted and briefly reviewed in this section.

Supposing the simulated material is isotropic within each α phase, the strain energy density $f_\varepsilon^{\Lambda_\alpha^\beta}$, at the surface Λ_α^β, is calculated as:

$$f_\varepsilon^{\Lambda_\alpha^\beta} = \frac{1}{2}\widetilde{\varepsilon}_i^{\Lambda_\alpha^\beta}\widetilde{K}_{ij}^\alpha\widetilde{\varepsilon}_j^{\Lambda_\alpha^\beta} = \frac{1}{2}\widetilde{\sigma}_i^{\Lambda_\alpha^\beta}\widetilde{\varepsilon}_i^{\Lambda_\alpha^\beta} \tag{34}$$

where the symmetric matrix $\widetilde{\boldsymbol{K}}^\alpha = \boldsymbol{M}_\sigma\overline{\boldsymbol{K}}^\alpha\boldsymbol{M}_\sigma^T$ is the transformed stiffness matrix, determining the relationship between the stresses $\widetilde{\boldsymbol{\sigma}}^\alpha$ and strains $\widetilde{\boldsymbol{\varepsilon}}^\alpha$ for the α phase.

After diffusing the sharp interface $\Lambda_{\alpha\beta}$ and introducing the concept of the order parameter $\boldsymbol{\phi}$, the strain energy density f_ε is calculated as:

$$f_\varepsilon = f_\varepsilon^\alpha h^\alpha(\boldsymbol{\phi}) + f_\varepsilon^\beta h^\beta(\boldsymbol{\phi}) = \frac{1}{2}\widetilde{\sigma}_i^\alpha\widetilde{\varepsilon}_i^\alpha h^\alpha(\boldsymbol{\phi}) + \frac{1}{2}\widetilde{\sigma}_i^\beta\widetilde{\varepsilon}_i^\beta h^\beta(\boldsymbol{\phi}) \tag{35}$$

where $\widetilde{\boldsymbol{\sigma}}^\alpha \approx \widetilde{\boldsymbol{\sigma}}^{\Lambda_\alpha^\beta}$, $\widetilde{\boldsymbol{\varepsilon}}^\alpha \approx \widetilde{\boldsymbol{\varepsilon}}^{\Lambda_\alpha^\beta}$ and $f_\varepsilon^\alpha \approx f_\varepsilon^{\Lambda_\alpha^\beta}$ when $0 < h^\alpha(\boldsymbol{\phi}) < 1$, since a thin diffuse interface is used to approximate the sharp interface. The influence of the diffuse interface width will be studied in Section 5.2.

Since only the sharp interface between two different phases is considered, the following equations can be obtained in accordance with Eqs. (2) and (4):

$$\phi_\beta = 1 - \phi_\alpha \tag{36a}$$

$$h^\beta(\boldsymbol{\phi}) = 1 - h^\alpha(\boldsymbol{\phi}) \tag{36b}$$

According to Eqs. (6) and (36a), the driving force in Eq. (5) can be simplified to:

$$\frac{1}{N}\sum_{\beta=1,\beta\neq\alpha}^{N}\left(\frac{\delta\mathcal{F}}{\delta\phi_\alpha} - \frac{\delta\mathcal{F}}{\delta\phi_\beta}\right) = \frac{\delta\mathcal{F}}{\delta\phi_\alpha} \tag{37}$$

Based on Eqs. (1), (6), (33), (36b) and (37), the driving force contributed by the strain energy density f_ε therefore is calculated as [23]:

$$\frac{\delta f_\varepsilon}{\delta\phi_\alpha} = \frac{\partial f_\varepsilon}{\partial\phi_\alpha} - \nabla\cdot\frac{\partial f_\varepsilon}{\partial\nabla\phi_\alpha} = \left(\varphi_\varepsilon^\alpha - \varphi_\varepsilon^\beta\right)\frac{\partial h^\alpha(\boldsymbol{\phi})}{\partial\phi_\alpha} \tag{38}$$

where $\varphi_\varepsilon^\alpha$ represents the strain potential for the α phase, which is calculated as follows[23]:

$$\varphi_\varepsilon^\alpha = \frac{1}{2}\widetilde{\sigma}_i^\alpha \widetilde{\varepsilon}_i^\alpha - \widetilde{\sigma}_i^{1\alpha}\widetilde{\varepsilon}_i^{1\alpha} = -\frac{1}{2}\widetilde{\sigma}_i^{1\alpha}\widetilde{\varepsilon}_i^{1\alpha} + \frac{1}{2}\widetilde{\sigma}_i^{2\alpha}\widetilde{\varepsilon}_i^{2\alpha} \tag{39}$$

The 6×6 stiffness matrix $\widetilde{\boldsymbol{K}}^\alpha$ is discretised into four 3×3 sub-matrices as follows:

$$\widetilde{\boldsymbol{\sigma}}^\alpha = \widetilde{\boldsymbol{K}}^\alpha \widetilde{\boldsymbol{\varepsilon}}^\alpha \implies \begin{pmatrix}\widetilde{\boldsymbol{\sigma}}^{1\alpha}\\ \widetilde{\boldsymbol{\sigma}}^{2\alpha}\end{pmatrix} = \begin{pmatrix}\widetilde{\boldsymbol{K}}^{11\alpha} & \widetilde{\boldsymbol{K}}^{12\alpha}\\ \widetilde{\boldsymbol{K}}^{21\alpha} & \widetilde{\boldsymbol{K}}^{22\alpha}\end{pmatrix}\begin{pmatrix}\widetilde{\boldsymbol{\varepsilon}}^{1\alpha}\\ \widetilde{\boldsymbol{\varepsilon}}^{2\alpha}\end{pmatrix} \tag{40}$$

Thus, Eq. (39) can be rewritten as:

$$\varphi_\varepsilon^\alpha(\widehat{\boldsymbol{\varepsilon}}^\alpha) = \frac{1}{2}\widehat{\varepsilon}_i^\alpha \widehat{K}_{ij}^\alpha \widehat{\varepsilon}_j^\alpha \tag{41}$$

where $\widehat{\boldsymbol{\varepsilon}}^\alpha = (\widetilde{\boldsymbol{\sigma}}^{1\alpha}, \widetilde{\boldsymbol{\varepsilon}}^{2\alpha})^T$, and

$$\widehat{\boldsymbol{\sigma}}^\alpha = (-\widetilde{\boldsymbol{\varepsilon}}^{1\alpha}, \widetilde{\boldsymbol{\sigma}}^{2\alpha})^T = \widehat{\boldsymbol{K}}^\alpha \widehat{\boldsymbol{\varepsilon}}^\alpha \tag{42}$$

with $\widehat{\boldsymbol{K}}^\alpha$ expressed as:

$$\widehat{\boldsymbol{K}}^\alpha = \begin{pmatrix} -(\widetilde{\boldsymbol{K}}^{11\alpha})' & (\widetilde{\boldsymbol{K}}^{11\alpha})'\widetilde{\boldsymbol{K}}^{12\alpha} \\ \widetilde{\boldsymbol{K}}^{21\alpha}(\widetilde{\boldsymbol{K}}^{11\alpha})' & \widetilde{\boldsymbol{K}}^{22\alpha} - \widetilde{\boldsymbol{K}}^{21\alpha}(\widetilde{\boldsymbol{K}}^{11\alpha})'\widetilde{\boldsymbol{K}}^{12\alpha}\end{pmatrix} \tag{43}$$

Eqs. (41) and (43) show that the strain potential $\varphi_\varepsilon^\alpha(\widehat{\boldsymbol{\varepsilon}}^\alpha)$ is expressed by $\widetilde{\boldsymbol{\sigma}}^{1\alpha}$ and $\widetilde{\boldsymbol{\varepsilon}}^{2\alpha}$, which respectively satisfy the jump condition in Eqs. (32b) and (32c), and that the stiffness matrix $\widehat{\boldsymbol{K}}^\alpha$ is symmetric. Therefore, the function $\Phi(\widehat{\boldsymbol{\varepsilon}}, \boldsymbol{\phi})$ can be constructed as:

$$\Phi(\widehat{\boldsymbol{\varepsilon}}, \boldsymbol{\phi}) = \varphi_\varepsilon^\alpha(\widehat{\boldsymbol{\varepsilon}})h^\alpha(\boldsymbol{\phi}) + \varphi_\varepsilon^\beta(\widehat{\boldsymbol{\varepsilon}})h^\beta(\boldsymbol{\phi}) = \frac{1}{2}\widehat{\varepsilon}_i \widehat{\mathcal{K}}_{ij}(\boldsymbol{\phi})\widehat{\varepsilon}_j \tag{44}$$

where $\widehat{\boldsymbol{\varepsilon}} = \widehat{\boldsymbol{\varepsilon}}^\alpha = \widehat{\boldsymbol{\varepsilon}}^\beta$, when $0 < h^\alpha(\boldsymbol{\phi}) < 1$. $\widehat{\boldsymbol{\mathcal{K}}}(\boldsymbol{\phi})$ is interpolated as:

$$\widehat{\mathcal{K}}_{ij}(\boldsymbol{\phi}) = \widehat{K}_{ij}^\alpha h^\alpha(\boldsymbol{\phi}) + \widehat{K}_{ij}^\beta h^\beta(\boldsymbol{\phi}) \tag{45}$$

Supposing $\widehat{\boldsymbol{\sigma}} = \widehat{\boldsymbol{\mathcal{K}}}(\boldsymbol{\phi})\widehat{\boldsymbol{\varepsilon}}$, the following equations can be derived according to Eqs. (38), (41), (42), (44) and (45):

$$\frac{\delta f_\varepsilon}{\delta \phi_\alpha} = \frac{\partial \Phi(\widehat{\boldsymbol{\varepsilon}}, \boldsymbol{\phi})}{\partial \phi_\alpha} \tag{46a}$$

$$\widehat{\boldsymbol{\sigma}} = \widehat{\boldsymbol{\sigma}}^\alpha h^\alpha(\boldsymbol{\phi}) + \widehat{\boldsymbol{\sigma}}^\beta h^\beta(\boldsymbol{\phi}) \tag{46b}$$

According to Eqs. (35), (42) and (46), it can be concluded that the jump of the variables $f_\varepsilon^{\Lambda_{\alpha\beta}}$, $(\widetilde{\boldsymbol{\varepsilon}}^1)^{\Lambda_{\alpha\beta}}$ and $(\widetilde{\boldsymbol{\sigma}}^2)^{\Lambda_{\alpha\beta}}$, which are related to the strain-energy-induced driving force, has been smoothly diffused with the function $h^\alpha(\boldsymbol{\phi})$.

Similar to the stiffness matrix $\widetilde{\boldsymbol{K}}^\alpha$, the 6×6 stiffness matrix $\widehat{\boldsymbol{\mathcal{K}}}$ is discretised into four 3×3 sub-matrices as follows:

$$\begin{pmatrix}\widehat{\boldsymbol{\sigma}}^1\\ \widehat{\boldsymbol{\sigma}}^2\end{pmatrix} = \begin{pmatrix}\widehat{\boldsymbol{\mathcal{K}}}^{11} & \widehat{\boldsymbol{\mathcal{K}}}^{12}\\ \widehat{\boldsymbol{\mathcal{K}}}^{21} & \widehat{\boldsymbol{\mathcal{K}}}^{22}\end{pmatrix}\begin{pmatrix}\widehat{\boldsymbol{\varepsilon}}^1\\ \widehat{\boldsymbol{\varepsilon}}^2\end{pmatrix} \tag{47}$$

Therefore, the relationship between the local effective stress fields $\widetilde{\boldsymbol{\sigma}} = (\widehat{\boldsymbol{\varepsilon}}^1, \widehat{\boldsymbol{\sigma}}^2)^T$ and the local effective strain fields $\widetilde{\boldsymbol{\varepsilon}} = (-\widehat{\boldsymbol{\sigma}}^1, \widehat{\boldsymbol{\varepsilon}}^2)^T$ can be derived as:

$$\begin{pmatrix}\widehat{\boldsymbol{\varepsilon}}^1\\ \widehat{\boldsymbol{\sigma}}^2\end{pmatrix} = \begin{pmatrix} -(\widehat{\boldsymbol{\mathcal{K}}}^{11})' & -(\widehat{\boldsymbol{\mathcal{K}}}^{11})'\widehat{\boldsymbol{\mathcal{K}}}^{12} \\ -\widehat{\boldsymbol{\mathcal{K}}}^{21}(\widehat{\boldsymbol{\mathcal{K}}}^{11})' & \widehat{\boldsymbol{\mathcal{K}}}^{22} - \widehat{\boldsymbol{\mathcal{K}}}^{21}(\widehat{\boldsymbol{\mathcal{K}}}^{11})'\widehat{\boldsymbol{\mathcal{K}}}^{12}\end{pmatrix}\begin{pmatrix}-\widehat{\boldsymbol{\sigma}}^1\\ \widehat{\varepsilon}^2\end{pmatrix} \tag{48}$$

which can be simplified to:

$$\widetilde{\boldsymbol{\sigma}}(\boldsymbol{x},t)=\widetilde{\boldsymbol{\mathcal{K}}}\widetilde{\boldsymbol{\varepsilon}}(\boldsymbol{x},t) \tag{49}$$

Now Eq. (49) is transformed into the global Cartesian coordinate system:

$$\boldsymbol{\sigma}(\boldsymbol{x},t)=\boldsymbol{K}\boldsymbol{\varepsilon}(\boldsymbol{x},t)=\boldsymbol{M}_{\varepsilon}^{T}\widetilde{\boldsymbol{\mathcal{K}}}\boldsymbol{M}_{\varepsilon}\boldsymbol{\varepsilon}(\boldsymbol{x},t) \tag{50}$$

where $\boldsymbol{\sigma}(\boldsymbol{x},t)$ and $\boldsymbol{\varepsilon}(\boldsymbol{x},t)$ are the effective stress and strain fields, respectively, in the Voigt notation. $\boldsymbol{K}$ is the effective stiffness matrix in Eq. (9).

It should be mentioned that the effective stiffness matrix $\boldsymbol{K}$ is exactly the same as the material stiffness matrix $\overline{\boldsymbol{K}}^{\alpha}$, when the interpolation function $h^{\alpha}(\boldsymbol{\phi})=1$. With Schneider et al.[23], the advantages of this interpolation scheme can be concluded as follows: (1) the interpolation scheme satisfies the mechanical jump condition, (2) the contribution of the elastic driving force is exactly equal to the elastic contribution of the Gibbs-Thomson equation, (3) both the interface width and the surface energy are stable at equilibrium and (4) the stress fields for the different phases are calculated at the diffuse interface, which is necessary to calculate the plastic strain fields according to the yield criterion.

4.2 Interpolation of density

In this section, the reciprocal of the effective density, i.e. $\mathcal{R}$ in Eq. (8), will be briefly derived, similar to the effective stiffness matrix $\boldsymbol{K}$.

At the surface Λ_{α}^{β}, the kinetic energy density $f_v^{\Lambda_{\alpha}^{\beta}}$ is calculated as:

$$f_v^{\Lambda_{\alpha}^{\beta}}=\frac{1}{2}v_i^{\Lambda_{\alpha}^{\beta}}\overline{\mathcal{M}}_{ij}^{\alpha}v_j^{\Lambda_{\alpha}^{\beta}}=\frac{1}{2}v_i^{\Lambda_{\alpha}^{\beta}}\psi_i^{\Lambda_{\alpha}^{\beta}} \tag{51}$$

where $\overline{\boldsymbol{\mathcal{M}}}^{\alpha}=diag(\rho_1^{\alpha},\rho_2^{\alpha},\rho_3^{\alpha})=diag(\rho^{\alpha},\rho^{\alpha},\rho^{\alpha})$, since the simulated material is supposed to be isotropic within a single-phase domain. $\boldsymbol{\psi}^{\Lambda_{\alpha}^{\beta}}=\overline{\boldsymbol{\mathcal{M}}}^{\alpha}\boldsymbol{v}^{\Lambda_{\alpha}^{\beta}}$ denotes the momentum fields at the surface Λ_{α}^{β}.

After diffusing the sharp interface $\Lambda_{\alpha\beta}$, the kinetic energy density is assembled as:

$$f_v=f_v^{\alpha}h^{\alpha}(\boldsymbol{\phi})+f_v^{\beta}h^{\beta}(\boldsymbol{\phi})=\frac{1}{2}v_i^{\alpha}\overline{\mathcal{M}}_{ij}^{\alpha}v_j^{\alpha}h^{\alpha}(\boldsymbol{\phi})+\frac{1}{2}v_i^{\beta}\overline{\mathcal{M}}_{ij}^{\beta}v_j^{\beta}h^{\beta}(\boldsymbol{\phi}) \tag{52}$$

where $\boldsymbol{v}^{\alpha}\approx\boldsymbol{v}^{\Lambda_{\alpha}^{\beta}}$, $\boldsymbol{\psi}^{\alpha}\approx\boldsymbol{\psi}^{\Lambda_{\alpha}^{\beta}}$ and $f_v^{\alpha}\approx f_v^{\Lambda_{\alpha}^{\beta}}$, when $0<h^{\alpha}(\boldsymbol{\phi})<1$. Thus, the driving force contributed by the kinetic energy density f_v is derived as:

$$\frac{\delta f_v}{\delta\phi_{\alpha}}=\frac{\partial f_v}{\partial\phi_{\alpha}}-\nabla\cdot\frac{\partial f_v}{\partial\nabla\phi_{\alpha}}=\left(f_v^{\alpha}-f_v^{\beta}\right)\frac{\partial h^{\alpha}(\boldsymbol{\phi})}{\partial\phi_{\alpha}} \tag{53}$$

It should be mentioned that it is not necessary to introduce a new function φ_v^{α} for this kinetic energy contribution, because all variables in $\boldsymbol{v}^{\alpha}$ satisfy the jump condition as demonstrated in Eq. (32d), which is not the case for the variables in $\widetilde{\boldsymbol{\varepsilon}}^{1\alpha}$. Correspondingly, the function $\Phi(\boldsymbol{v},\boldsymbol{\phi})$ is constructed as:

$$\Phi(\boldsymbol{v},\boldsymbol{\phi})=f_v^{\alpha}(\boldsymbol{v})h^{\alpha}(\boldsymbol{\phi})+f_v^{\beta}(\boldsymbol{v})h^{\beta}(\boldsymbol{\phi})=\frac{1}{2}v_i\mathcal{M}_{ij}(\boldsymbol{\phi})v_j \tag{54}$$

where $\boldsymbol{v}=\boldsymbol{v}^{\alpha}=\boldsymbol{v}^{\beta}$, when $0<h^{\alpha}(\boldsymbol{\phi})<1$. $\boldsymbol{\mathcal{M}}(\boldsymbol{\phi})$ is the effective density matrix, which is interpolated as:

$$\mathcal{M}_{ij}(\boldsymbol{\phi})=\overline{\mathcal{M}}_{ij}^{\alpha}h^{\alpha}(\boldsymbol{\phi})+\overline{\mathcal{M}}_{ij}^{\beta}h^{\beta}(\boldsymbol{\phi}) \tag{55}$$

Supposing $\boldsymbol{\psi}=\boldsymbol{\mathcal{M}}(\boldsymbol{\phi})\boldsymbol{v}$, the following equations can be derived according to Eqs. (53), (54) and (55):

$$\frac{\delta f_v}{\delta \phi_\alpha} = \frac{\partial \Phi(\boldsymbol{v}, \boldsymbol{\phi})}{\partial \phi_\alpha} \tag{56a}$$

$$\boldsymbol{\psi} = \boldsymbol{\psi}^\alpha h^\alpha(\boldsymbol{\phi}) + \boldsymbol{\psi}^\beta h^\beta(\boldsymbol{\phi}) \tag{56b}$$

Thus, it can be concluded that the jump of the variables $f_v^{\Lambda_{\alpha\beta}}$ and $\boldsymbol{\psi}^{\Lambda_{\alpha\beta}}$, which are related to the driving force induced by the kinetic energy, has been smoothly diffused with the function $h^\alpha(\boldsymbol{\phi})$.

It can be observed that the effective density matrix $\boldsymbol{\mathcal{M}}$ is a diagonal matrix, with $\mathcal{M}_{11} = \mathcal{M}_{22} = \mathcal{M}_{33}$. Furthermore, the values of the diagonal elements in the matrix $\boldsymbol{\mathcal{M}}$ are equal to ρ^α when $h^\alpha(\boldsymbol{\phi}) = 1$. According to Eq. (55), the reciprocal of the effective density, $\mathcal{R}$ in Eq. (8), therefore is calculated as:

$$\mathcal{R} = \frac{1}{\rho^\alpha h^\alpha(\boldsymbol{\phi}) + \rho^\beta h^\beta(\boldsymbol{\phi})} \tag{57}$$

5 Numerical validations

In this section, the numerical methods introduced in Section 2, the jump condition at the sharp interface derived in Section 3, the numerical accuracy of the interpolation scheme presented in Section 4 and the application efficiency in the multiphase system are investigated on the basis of the code developed on the platform of PACE3D. The polynomial degree q in Eq. (12) is fixed as 3, in all the numerical examples.

5.1 Validation 1: jump condition at the sharp interface

According to Eq. (32), two numerical examples are established, as illustrated in Figure 6. The first one, namely Example 1, is a $1\mu m \times 200\mu m \times 1\mu m$ beam and discretised into 200 cells, while the second one, Example 2, is $1\mu m \times 100\mu m \times 20\mu m$ and discretised into 2000 cells. For both examples, the cell size is $1\mu m \times 1\mu m \times 1\mu m$. The origin of the Cartesian coordinate system is located at the left-bottom-back corner of the beam, such that the simulated domains for the two examples are $[(0, 0, 0), (1, 200, 1)]$ and $[(0, 0, 0), (1, 100, 20)]$, respectively. In order to validate the jump condition derived in Section 3, the simulated domains are divided into two equally dimensioned phases, i.e. phases α and β, through sharp interfaces, as shown in Figure 6. In each example, the two different waveforms in Figure 5 are applied as incident waves at the left-side surface $x_2 = 0$, which is defined as a free boundary. In both examples, the surfaces on the right side are designed as nonreflective boundaries, while the other four surfaces in each example are de-dimension boundaries.

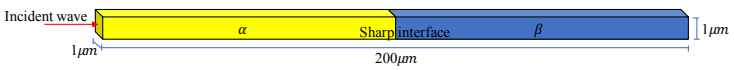

(a) Example 1

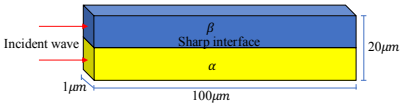

(b) Example 2

Figure 6: Numerical examples with a sharp interface

Based on Eq. (32) and the geometrical symmetry of the two examples, two different incident waves, i.e. σ_{22} and σ_{12}, are applied and studied for each example with each

wave type. However, it should be pointed out that the stresses σ_{22} and σ_{12} in Example 1 are normal components to the sharp interface, while they are tangential components in Example 2. In order to gain an insight into the jump condition at the sharp interfaces with quasi-1D examples, the material properties and incident waves for the α and β phases are specially designed, as illustrated in Table 1. It is observed that the first Lamé parameter λ is fixed as 0, that the second Lamé parameter μ, the density ρ and the stress amplitude $|\sigma|_{\max}$ of the incident waves are not equal for the α and β phases, and that the propagation velocities of the elastic wave, however, are equal for the α and β phases, which are calculated as:

$$\mathcal{V}_P^\alpha = \sqrt{\frac{\lambda^\alpha + 2\mu^\alpha}{\rho^\alpha}} \qquad \mathcal{V}_S^\alpha = \sqrt{\frac{\mu^\alpha}{\rho^\alpha}} \tag{58}$$

where $\mathcal{V}_P^\alpha$ and $\mathcal{V}_S^\alpha$ are the respective P-wave (primary wave) and S-wave (secondary wave) velocities for the α phase.

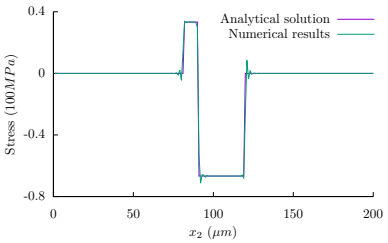

(a) Stress field σ_{22} at $t = 20.40ns$

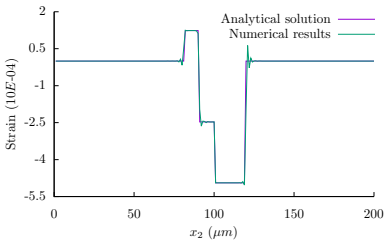

(b) Strain field ε_{22} at $t = 20.40ns$

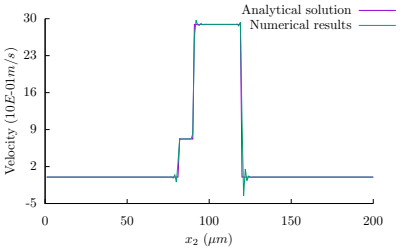

(c) Velocity field v_2 at $t = 20.40ns$

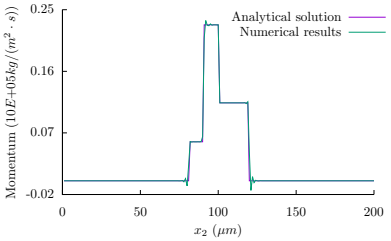

(d) Momentum field ψ_2 at $t = 20.40ns$

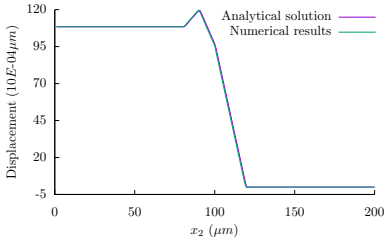

(e) Displacement field w_2 at $t = 20.40ns$

Figure 7: Mechanical fields for the Type I P-wave in Example 1 with a sharp interface

The frequency of the incident stress waves is $200MHz$, and the timestep Δt is set to $0.01ns$. To avoid tediousness, only some numerical results of displacement, stress, strain, velocity and momentum waveforms are selected as representatives for Examples 1 and 2 and are illustrated in Figures 7-10, which also provide the visual comparison

Table 1: Material properties and incident waves for the α and β phases

Phase	$\lambda(GPa)$	$\mu(GPa)$	$\rho(kg/m^3)$	$\mathcal{V}_P(m/s)$	$\mathcal{V}_S(m/s)$	$\lvert\sigma\rvert_{\max}(100MPa)$	
						Example 1	Example 2
α	0	134.9	7880	5851.37	4137.55	1	1
β	0	67.45	3940	5851.37	4137.55	-	0.5

between the numerical results and the analytical solution. For every waveform of each numerical example, the L_2-norm relative error is additionally calculated and presented in Table 2.

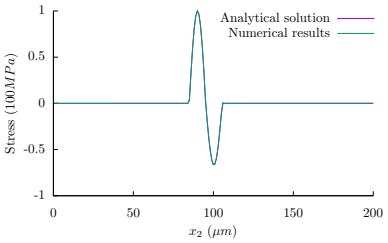

(a) Stress field σ_{12} at $t = 25.40ns$

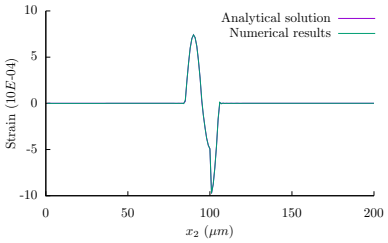

(b) Strain field ε_{12} at $t = 25.40ns$

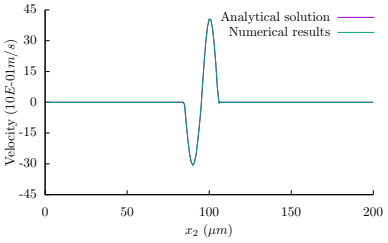

(c) Velocity field v_1 at $t = 25.40ns$

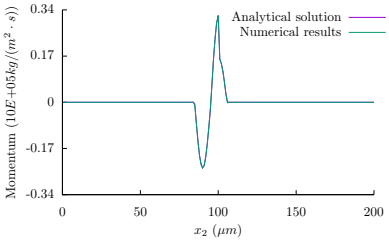

(d) Momentum field ψ_1 at $t = 25.40ns$

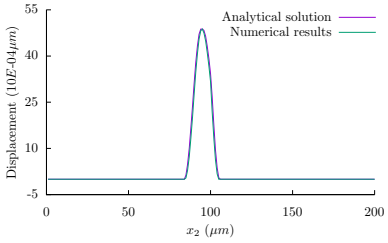

(e) Displacement field w_1 at $t = 25.40ns$

Figure 8: Mechanical fields for the Type II S-wave in Example 1 with a sharp interface

From Figures 7-10, the following conclusions can be drawn: (1) In both examples, the numerical results for all mechanical fields agree well with the analytical solution, although there are small fluctuations for the Type I wave, which are due to the strong discontinuity property. (2) The jump conditions for both wave types, described by Eqs. (32a) and (32d), are validated through both examples, while the jump conditions described by Eqs. (32b) and (32c) are validated through Example 1 and Example 2, respectively. (3) Despite the jump condition specified by Eq. (32), the continuity property stated in Proposition 1 cannot be ensured for the Type I wave, which can be

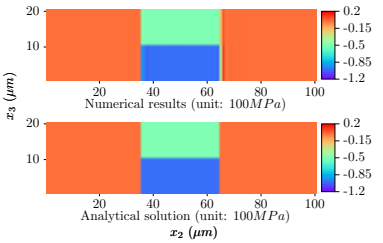

(a) Stress field σ_{12} at $t = 11.00ns$

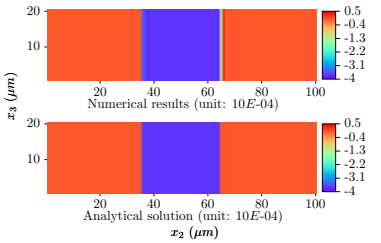

(b) Strain field ε_{12} at $t = 11.00ns$

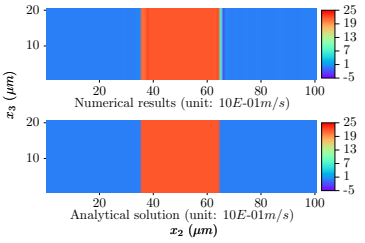

(c) Velocity field v_1 at $t = 11.00ns$

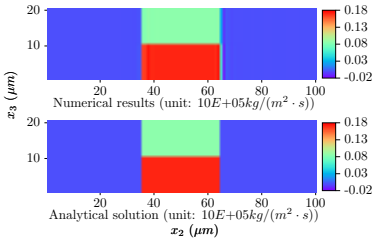

(d) Momentum field ψ_1 at $t = 11.00ns$

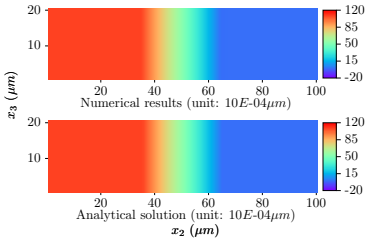

(e) Displacement field w_1 at $t = 11.00ns$

Figure 9: Mechanical fields for the Type I P-wave in Example 2 with a sharp interface

Table 2: L_2-norm relative error for each waveform in Examples 1 and 2 (%)

Example	1				2			
Type	P-wave		S-wave		P-wave		S-wave	
	I	II	I	II	I	II	I	II
Time (ns)	20.40	18.30	27.50	25.40	11.00	11.00	15.00	15.00
Displacement	2.33	5.82	3.15	8.04	3.18	6.37	4.32	8.93
Stress	4.05	0.50	6.60	1.46	1.54	0.37	7.95	0.55
Strain	2.44	0.46	6.28	1.26	1.54	0.37	7.95	0.55
Velocity	1.79	0.80	5.72	1.58	1.22	0.93	7.44	1.09
Momentum	2.45	0.75	4.81	1.69	1.22	0.93	7.44	1.09

concluded from Figures 7 and 9.

From Table 2, it can be concluded that the numerical errors of the stress, strain, velocity and momentum fields are greater for the Type I wave than for the Type II wave, which is due to the strong discontinuity at the beginning and the end of the Type I wave. However, the numerical errors of the displacement fields are greater for the Type II wave, since the analytical solutions for the Type I and Type II waves are

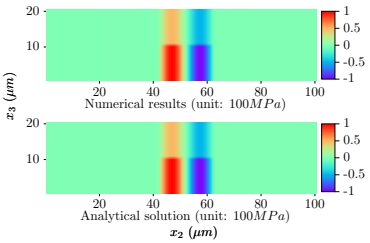

(a) Stress field σ_{12} at $t = 15.00ns$

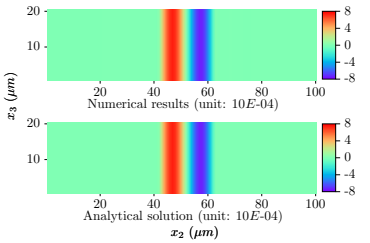

(b) Strain field ε_{12} at $t = 15.00ns$

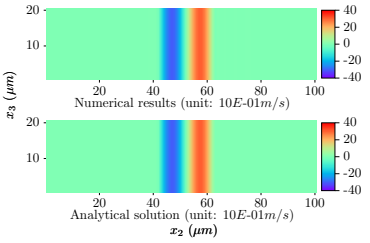

(c) Velocity field v_1 at $t = 15.00ns$

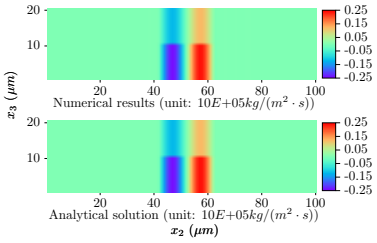

(d) Momentum field ψ_1 at $t = 15.00ns$

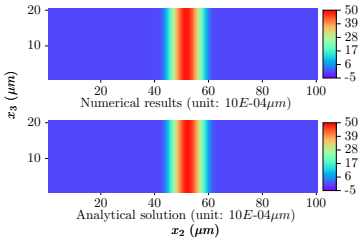

(e) Displacement field w_1 at $t = 15.00ns$

Figure 10: Mechanical fields for the Type II S-wave in Example 2 with a sharp interface

linear and cosinoidal functions, respectively, both of which are continuous over the whole domain. The values from the same numerical example show that the numerical errors of the S-wave are greater than those of the P-wave, because the length of the S-wave is shorter.

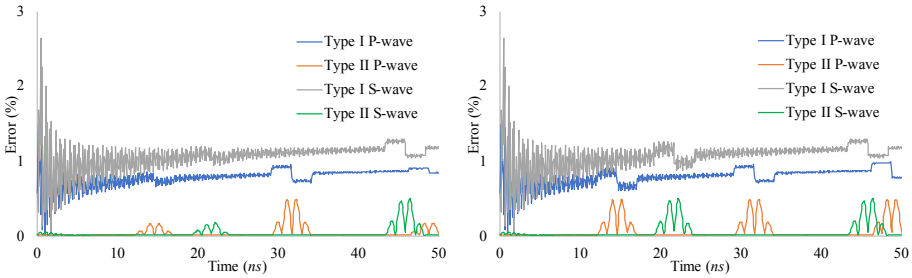

(a) The error in Example 1

(b) The error in Example 2

Figure 11: The error of the total mechanical energy in the whole simulated domain

Then, the surfaces on the right side of both examples are changed into free boundaries. For a period of $50ns$ after the end of loading, the total mechanical energy of the whole simulated domain is compared with the corresponding analytical solution, and the error is presented in Figure 11. For all cases, it is observed that the maximum error is less than 3%. Moreover, the error for the cases with a Type I wave generally converges to 1%, while it is almost zero for the cases with a Type II wave.

5.2 Validation 2: interpolation scheme

In this subsection, the sharp interfaces in Examples 1 and 2 are approximated through diffuse interfaces, as illustrated in Figure 12.

In order to study the influence of the wavelength upon the interpolation scheme introduced in Section 4, the length in the x_2 direction is designed differently for Example 3 in Figure 12a, which is in accordance with the frequencies of the incident waves, as listed in Table 3. The lengths in the x_1 and x_3 directions are kept as $1\mu m$. The material properties for the α and β phases and the stress amplitude $|\sigma|_{\max}$ of the incident wave remain the same as in Example 1.

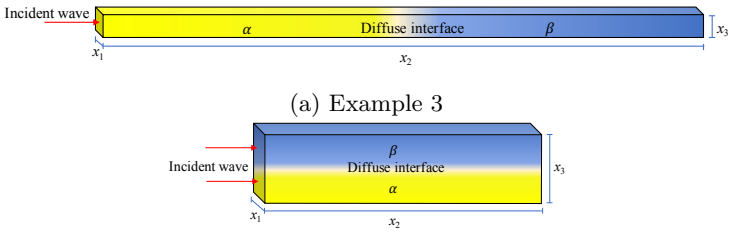

(a) Example 3

(b) Example 4

Figure 12: Numerical examples with a diffuse interface

Table 3: Lengths in the x_2 direction, for the different incident-wave frequencies in Example 3

Frequency (MHz)		200	100	50	20	10
x_2 (μm)	P-wave	150	200	300	800	1500
	S-wave	150	200	300	600	1000

For the frequency with the value of $50MHz$, the numerical results of the waveforms induced by the Type II P-wave and the Type I S-wave are visually presented and compared with the analytical sharp-interface solution in Figures 13 and 14, respectively, both of which include the reflected and transmitted stress and velocity waveforms, as well as the strain and momentum waveforms at the diffuse interface. It is observed that the numerical results of all waveforms generally agree well with the analytical sharp-interface solution. The lengths of the reflected waves become longer for both wave types, since the sharp interface with infinitesimal thickness is approximated through a diffuse interface with finite thickness. As a consequence, the amplitudes of the reflected Type II sinusoidal wave become smaller according to the conservation law of energy, which is not the case for the reflected Type I square wave, since the duration of its peak value lasts longer. With the interpolation scheme presented in Section 4, the values of the strain and momentum waveforms located within the diffuse interface vary gradually, similar to the volume fraction curves in Figure 1, which coincides with the conclusion in Schneider et al. [23].

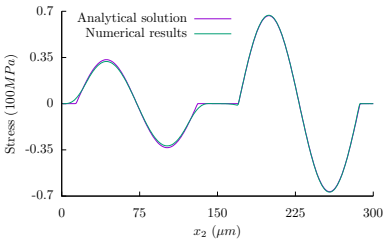

(a) Stress field σ_{22} at $t = 49.00ns$

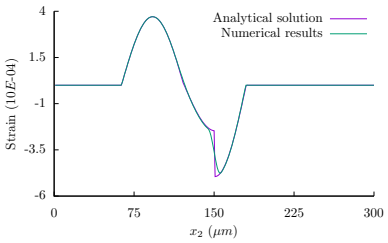

(b) Strain field ε_{22} at $t = 30.70ns$

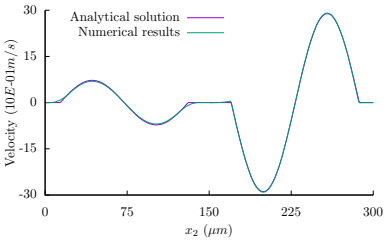

(c) Velocity field v_2 at $t = 49.00ns$

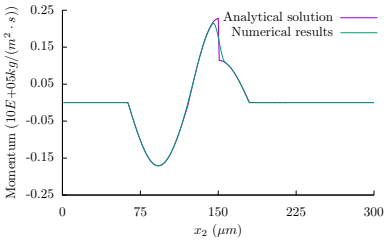

(d) Momentum field ψ_2 at $t = 30.70ns$

Figure 13: Mechanical fields for the Type II P-wave in Example 3, with a frequency of $50MHz$ and a diffuse interface

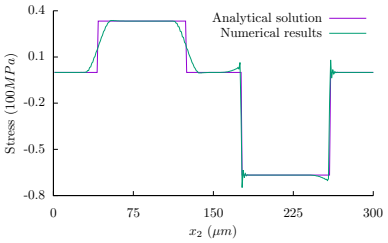

(a) Stress field σ_{12} at $t = 62.50ns$

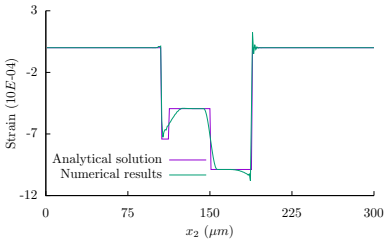

(b) Strain field ε_{12} at $t = 45.40ns$

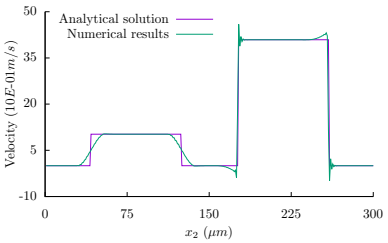

(c) Velocity field v_1 at $t = 62.50ns$

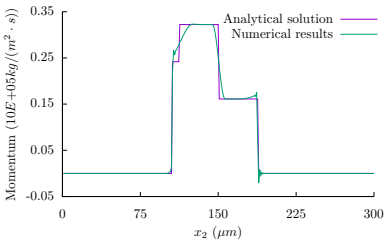

(d) Momentum field ψ_1 at $t = 45.40ns$

Figure 14: Mechanical fields for the Type I S-wave in Example 3, with a frequency of $50MHz$ and a diffuse interface

Since the numerical errors of the reflected waveforms are induced by approximating the sharp interface with infinitesimal thickness with the diffuse interface with finite thickness, the errors of the reflected and transmitted wavelength and stress amplitude are plotted against the ratio between the incident wavelength and the diffuse interface

length, as demonstrated in Figure 15. It can be concluded that the errors of the transmitted waveforms are negligible, since most of them are less than 5%. The errors of the reflected wavelength decrease dramatically, when increasing the ratio. The errors of the reflected wavelength are larger for the Type I wave than for the Type II wave, which is due to the strong discontinuity property. The errors of the reflected stress amplitude are greater for the Type II sinusoidal wave than for the Type I square wave, especially when the ratio is less than 20, because the duration of the peak value lasts longer in the Type I square wave. In Figure 15b, it is important to note that the numerical errors of the stress amplitude are selected as representative, since the strain, velocity and momentum waveforms can be derived according to the stress waveform.

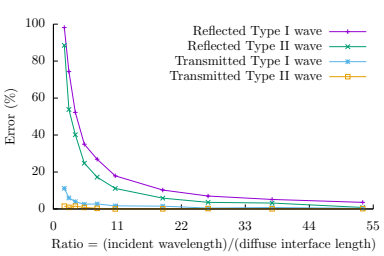

(a) Numerical errors of the wavelength

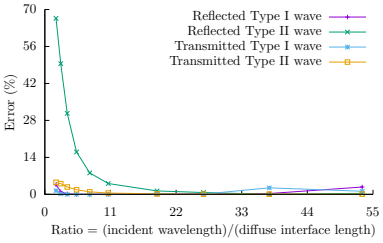

(b) Numerical errors of the stress amplitude

Figure 15: The influence of the ratio between the incident wavelength and the diffuse interface length upon the numerical errors of the wavelength and the stress amplitude

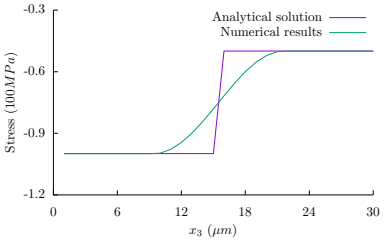

(a) Stress field σ_{22} at $x_2 = 55\mu m, t = 10.60ns$

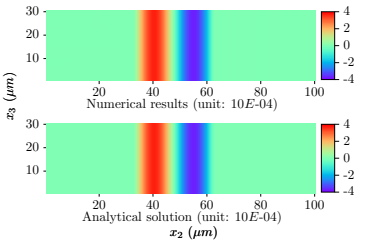

(b) Strain field ε_{22} at $t = 10.60ns$

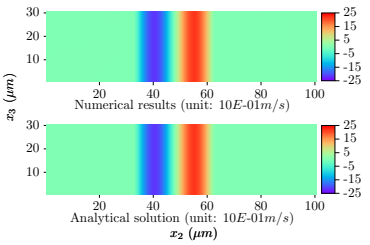

(c) Velocity field v_2 at $t = 10.60ns$

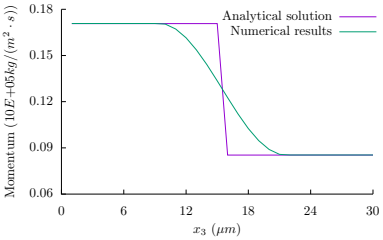

(d) Momentum field ψ_2 at $x_2 = 55\mu m, t = 10.60ns$

Figure 16: Mechanical fields for the Type II P-wave in Example 4, with a frequency of $200MHz$ and a diffuse interface

For Example 4 in Figure 12b, the parameters for the material property and the incident wave remain the same as for Example 2. To get a better insight into the mechanical fields across the diffuse interface, the geometrical dimensions are changed into $1\mu m \times 100\mu m \times 30\mu m$.

For the Type II P-wave and the Type I S-wave with a frequency of $200MHz$, the stress and momentum fields across the diffuse interface and the strain and velocity fields over the whole simulated domain are illustrated in Figures 16 and 17, where they are compared with the analytical sharp-interface solution. The following observations are made: (1) With the interpolation scheme introduced in Section 4, the values of the stress and the momentum fields vary gradually across the diffuse interface, similar to the volume fraction curves in Figure 1, which again coincides with the conclusion made in Schneider et al.[23]. (2) The strain and velocity fields agree well with the analytical sharp-interface solution, whose L_2-norm relative errors are the same as those in Table 2. Thus, it can be concluded that the interpolation scheme derived in Section 4 prevents an increase of numerical error, which is usually caused by approximating the sharp interface with infinitesimal thickness with the diffuse interface with finite thickness in Example 4, i.e. the case where a wave propagates parallel to the interface.

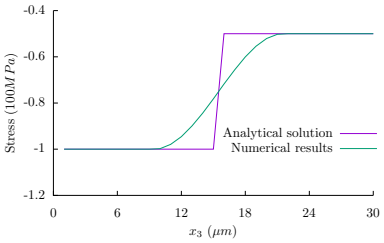

(a) Stress field σ_{12} at $x_2 = 50\mu m, t = 14.30ns$

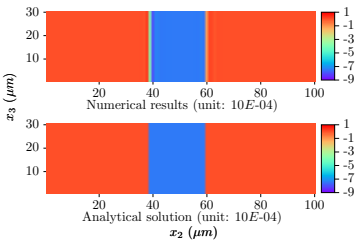

(b) Strain field ε_{12} at $t = 14.30ns$

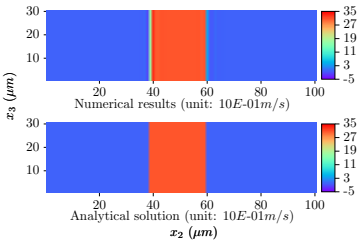

(c) Velocity field v_1 at $t = 14.30ns$

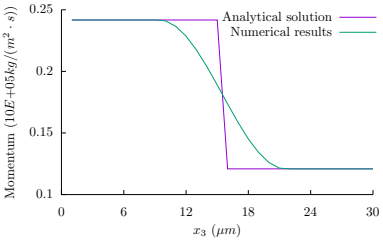

(d) Momentum field ψ_1 at $x_2 = 50\mu m, t = 14.30ns$

Figure 17: Mechanical fields for the Type I S-wave in Example 4, with a frequency of $200MHz$ and a diffuse interface

As the examples in Subsection 5.1, the surfaces on the right side of Examples 3 and 4 are reset as free boundaries. After the end of loading, the error of total mechanical energy within $50ns$ is presented in Figure 18, by comparing with the analytical solution. It is observed that the maximum error is less than 2% for Example 3 and less than 3% for Example 4. The errors for almost all Type I wave cases converge to the values around or below 1%, while the errors for all Type II wave cases are almost zero.

Based on the analysis of the numerical results in Subsections 5.1 and 5.2, it is therefore suggested that the ratio between the minimum wavelength and the maximum diffuse interface length should be greater than 30 in a multiphase system.

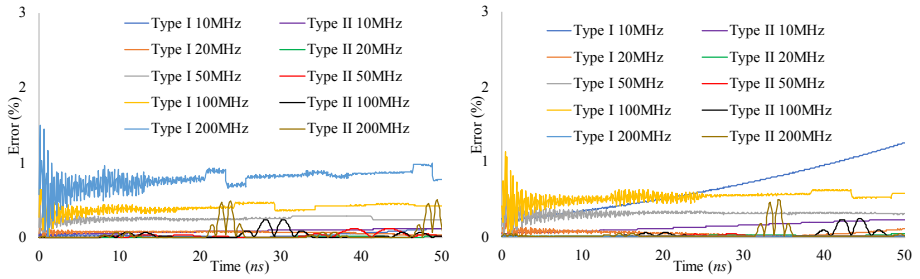

(a) The error for the P-wave in Example 3 (b) The error for the S-wave in Example 3

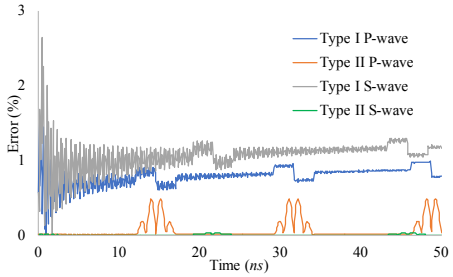

(c) The error in Example 4

Figure 18: The error of the total mechanical energy in the whole simulated domain

5.3 Validation 3: 2D simulation with two phases

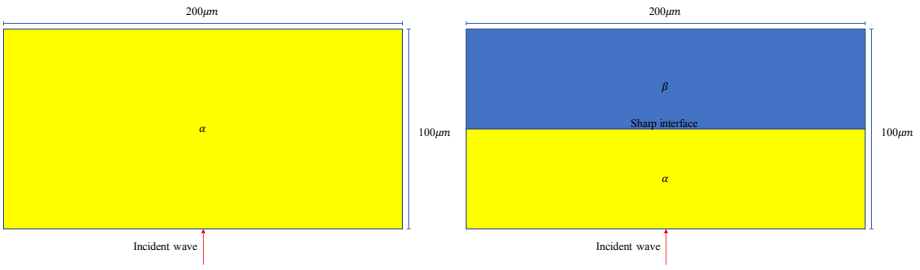

(a) Example 5a (b) Example 5b

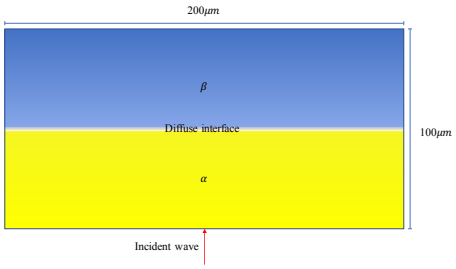

(c) Example 5c

Figure 19: A 2D numerical example with two different phases

As illustrated in Figure 19, a 2D numerical example, i.e. Example 5, with different

phase information is simulated and analysed. The dimension of Example 5 is $1\mu m \times 200\mu m \times 100\mu m$, which is designed as a single-phase (α phase) domain in Example 5a, while it is equally discretised into two phases, α and β, through a sharp interface in Example 5b and a diffuse interface in Example 5c. The material properties for these two phases are listed in Table 4. The Type I wave in Figure 5b, with a frequency of $50MHz$ and a stress amplitude of $100MPa$, is loaded at the bottom surface of the cell $[(0, 100, 0), (1, 101, 1)]$. The surfaces normal to the x_1 direction are set as de-dimension boundaries, the bottom surface is set as a free boundary and the remaining surfaces are set as nonreflective boundaries.

Table 4: Material properties for the different phases in Subsections 5.3 and 5.4

Phase	$\lambda(GPa)$	$\mu(GPa)$	$\rho(kg/m^3)$	$\mathcal{V}_P(m/s)$	$\mathcal{V}_S(m/s)$
α	105	82.4	5910	6756.58	3733.96
β	26.25	20.6	7880	2925.69	1616.85
γ	52.5	41.2	6304	4625.92	2556.47

Table 5: Properties of the mechanical fields, with respect to the sharp interface between the α and β phases

Property	σ_{33}	ε_{33}	σ_{22}	ε_{22}	v_2	ψ_2
Normal	✓	✓				
Tangential			✓	✓	✓	✓
Continuous	✓			✓	✓	

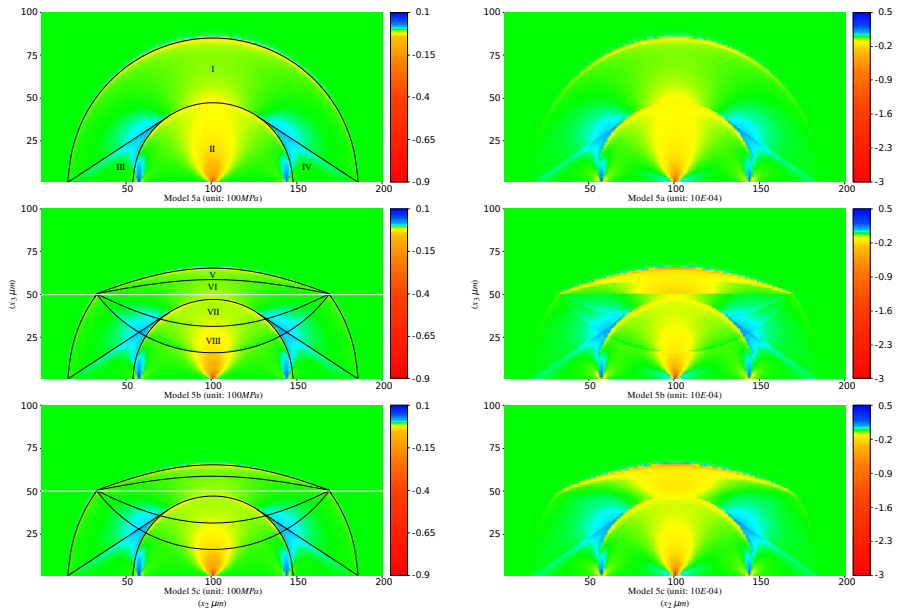

(a) Stress field σ_{33} (b) Strain field ε_{33}

Figure 20: Comparison of the stress field σ_{33} and the strain field ε_{33}

When time $t = 12.50ns$, the numerical results of several selected stress, strain, velocity and momentum fields are taken from three different examples and are compared

in Figures 20-22. With respect to the sharp interface between the α and β phases, the directional properties and continuity of these mechanical fields are listed in Table 5.

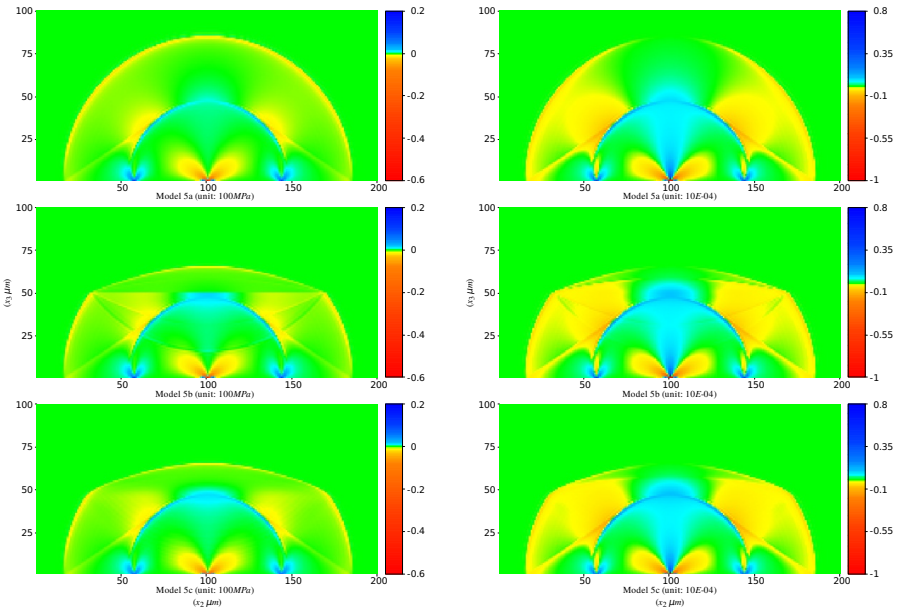

(a) Stress field σ_{22} (b) Strain field ε_{22}

Figure 21: Comparison of the stress field σ_{22} and the strain field ε_{22}

Additionally, the analytical solutions for different region boundaries are plotted in Figure 20a, together with the white-coloured horizontal line denoting the interface. The boundaries of four different wave regions, as derived by Fung[49], are plotted in the top image of Figure 20a. Within this single-phase domain, the P-wave generated by the incident wave exists in all four regions, while the S-wave generated by the incident wave only occupies Region II. When the wave front of the P-wave intersects with the free boundary, the intersection points can additionally be analysed as new wave sources, which generate both P- and S-waves. The P-wave, generated by the new wave sources, disturbs all four regions, while the newly generated S-wave on the left propagates through the Regions II and III, and the newly generated S-wave on the right occupies the Regions II and IV. When the simulated domain is discretised into two equally dimensioned areas by means of a sharp interface, as shown in Figure 19b, four more new regions are generated by the transmission and reflection of the P-wave at the sharp interface, as illustrated in the middle image of Figure 20a. Through the calculation with the incident angle, the refraction angle and the reflection angle, the transmitted P-wave exists in the Regions V and VI, while the reflected P-wave is present in the Regions VII and VIII. Moreover, the new S-wave is also generated, due to the intersection of the P-wave and the material interface. The transmitted S-wave occupies Region VI, while the reflected S-wave disturbs Region VII. It is worth mentioning that more new regions will be generated, when the S-wave in Regions II, III and IV intersects with the sharp interface. Therefore, when time $t = 12.50ns$, there are mainly eight regions, as shown in Figure 20a. According to the numerical results demonstrated in Figure 14, when the sharp interface is replaced by the diffuse interface as illustrated in 19c, it can be predicted that (1) the wave fronts not yet intersecting with the interface and the wave fronts of the transmitted waves can be observed, (2) that the wave fronts of the reflected waves are diffused by the diffuse interface and (3)

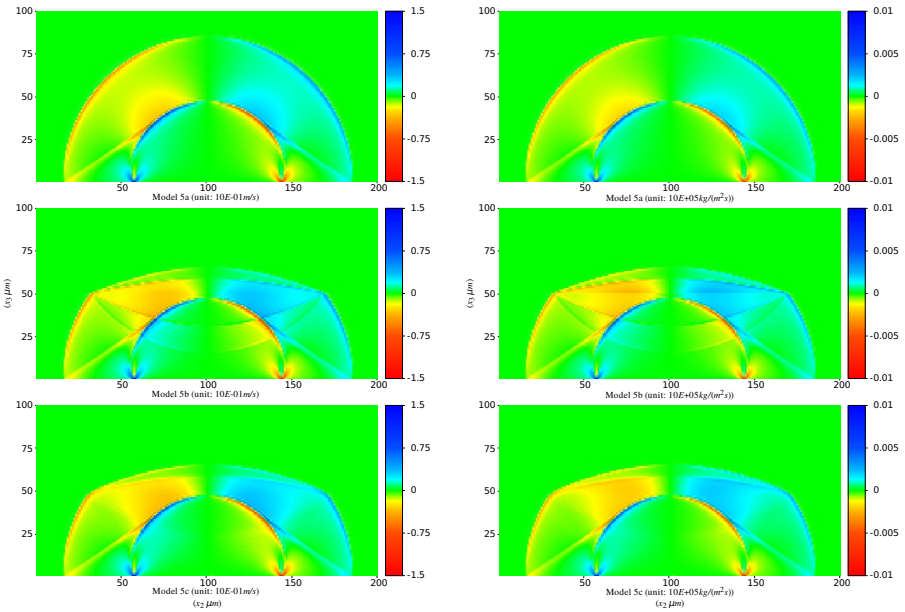

(a) Velocity field v_2 (b) Momentum field ψ_2

Figure 22: Comparison of the velocity field v_2 and the momentum field ψ_2

that the mechanical fields, which are discontinuous at the sharp interface, are diffused with the order parameters ϕ_α and ϕ_β.

In Figures 20-22, it is observed that almost all four/eight wave regions can be clearly distinguished in Examples 5a and 5b, except those whose values do not jump wide enough to demonstrate the wave fronts. In addition, the wave fronts in Example 5c agree well with the prediction at the end of the previous paragraph. For the numerical results from Example 5b, the mechanical fields σ_{33}, ε_{22} and v_2 are continuous across the sharp interface, as listed in Table 5, while the jump of all remaining mechanical fields, i.e. ε_{33}, σ_{22} and ψ_2, is clearly observed. For the numerical results from Example 5c, all mechanical fields which are continuous at the sharp interface are retained as continuous, while the discontinuous fields are successfully diffused by the order parameters ϕ_α and ϕ_β.

5.4 Multiphase system

A numerical multiphase example with diffuse interfaces is established, as shown in Figure 23, where the geometrical dimension, the boundary condition and the loading condition are equal to Example 5 in Figure 19, except that the loading period in this multiphase system is set to $t > 0$. For the convenience of analysing the numerical results, several areas demarcated by phase interfaces are labelled with Roman numerals, which will be referred to as Area I, II ..., to distinguish them from the regions in Figure 20a, as shown in Figure 23. The material properties for the different phases are listed in Table 4. It is worth noticing that the propagation velocities for the α phase are highest, while they are lowest for the β phase.

At time $t = 3.50ns, 10.00ns, 20.00ns$ and $30.00ns$, the numerical results for the stress field σ_{33}, the strain field ε_{23}, the velocity field v_3 and the momentum field ψ_2 are respectively presented in Figure 24. In Figure 24a, the Regions I-IV, described in Figure 20a, are clearly observed. However, the mechanical wave propagates faster

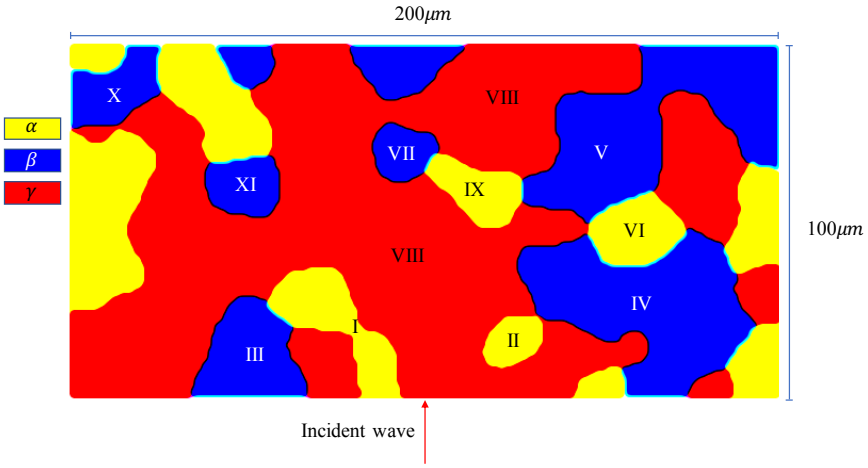

Figure 23: A numerical multiphase example

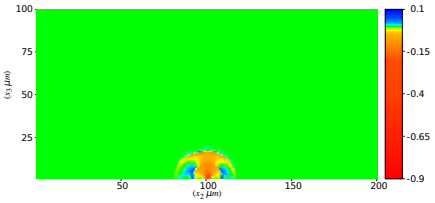

(a) Stress field σ_{33} at $t = 3.50ns$ (unit: $100MPa$)

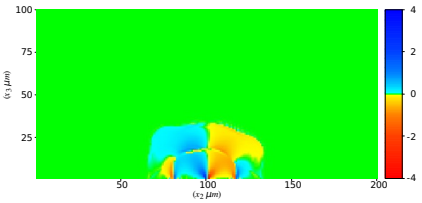

(b) Strain field ε_{23} at $t = 10.00ns$ (unit: $10E$-04)

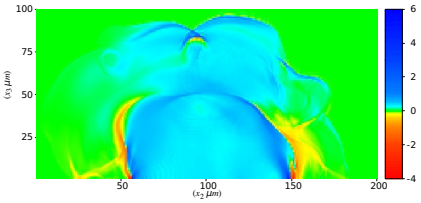

(c) Velocity field v_3 at $t = 20.00ns$ (unit: $10E$-$01m/s$)

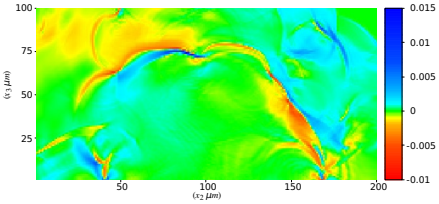

(d) Momentum field ψ_2 at $t = 30.00ns$ (unit: $10E$+$05kg/(m^2 \cdot s)$)

Figure 24: Mechanical fields in the numerical multiphase example with diffuse interfaces

towards the left than towards the right, since the propagation velocities in Area I, which is filled with the α phase, are the highest among the three different phases. Similarly, the mechanical wave in Figure 24b propagates faster in the upper-left and upper-right directions, which is due to the existence of the Areas I and II. In Figure 24c, it is observed that the mechanical wave on the lower-left side propagates slower after reaching Area III. On the right side, the mechanical wave going from the middle towards the upper-right direction propagates slower than the one going from the top towards the upper side and the one going from the bottom towards the right side, which is because of Areas IV and V. However, the wave front passing through Area VI propagates further than its surroundings, due to the highest propagation velocities of the α phase. The phenomenon of diffraction is clearly observed at the top of Area

VII, since some parts of the mechanical wave bypass Area VII through Areas VIII and IX. In Figure 24d, the mechanical field becomes more complicated, due to the different propagation velocities of the different phases and the reflection/transmission at the interfaces. However, within Area X and the lower left of Area V, two clusters of the mechanical wave are still observed. The former is mainly caused by the diffraction phenomenon around Area XI, while the latter is mainly due to the wave transmission and reflection from its surrounding areas.

In this multiphase system, the diffuse interfaces between the different phases are generated as curves with finite thickness. This means that the normal vectors of the interfaces may be oriented in any direction. Therefore, according to the jump condition in Eq. (32) and the material properties in Table 4, there are discontinuities within the entire stress field σ_{33}, strain field ε_{23} and momentum field ψ_2 of the corresponding sharp-interface system. From Figure 24, it can be concluded that the interpolation scheme derived in Section 4 has successfully diffused the jumps of the mechanical fields.

6 Conclusions

In order to investigate the influence of the mechanical wave upon the process of the microstructural evolution, high-order DGM is embedded into the multifunctional numerical analysis software PACE3D. In PACE3D, the free energy is calculated by stress, strain, velocity, momentum and other fields, together with the order parameter $\phi_\alpha(\boldsymbol{x}, t)$, which represents the volume fraction of the α phase at the location $\boldsymbol{x}$ and the time t. Thus, the evolution of the α phase is characterised by the evolution of the order parameter ϕ_α, whose driving force is formulated by the derivation of free energy with respect to the order parameter ϕ_α and the gradient of the order parameter $\nabla\phi_\alpha$. Thus, the effort necessary for tracking the interfaces among different phases is obviated. In order to obtain the driving force, the free energy at the sharp interface should be correctly interpolated with the N-tuple $\boldsymbol{\phi}$, which replaces the sharp interface with a diffuse interface.

In this paper, the jump condition and continuity property of mechanical fields are therefore investigated at the sharp interface, with regard to the mechanical waves with strong discontinuity (Type I wave) and weak discontinuity (Type II wave). Based on the observed jump condition, the interpolation scheme for the stiffness matrix and the density at the diffuse interface is derived. With the interpolation scheme and the Type I and Type II incident waves, several numerical examples are carried out. By comparing the numerical results and the analytical solutions, the following conclusions are drawn: (1) Generally, the numerical results for the mechanical wave propagation, the transmission and the reflection agree well with the analytical solutions. (2) The numerical results from the examples with a sharp interface exactly verify the jump conditions described by Eq. (32). (3) With the interpolation scheme, the jump of the discontinuous mechanical fields is correctly diffused in the examples with a diffuse interface. (4) It is suggested that the ratio between the minimum wavelength and the maximum diffuse interface length should be greater than 30 in a multiphase system. (5) According to the analysis of the numerical results in the multiphase system, it is verified that the simulation scheme presented in this paper is accurate and efficient, and ready for the application to microstructural evolution by providing the formula of the driving force contributed by the mechanical wave.

However, it is worth pointing out that the current simulation scheme is derived on the basis of the assumption of an infinitesimal deformation. The formula for the finite deformation should be further developed and verified in the future, in order to extend the application scope. Then, the driving forces will be calculated with the sharp interface limit, to simulate phase transformation under the mechanical wave propagation.

Acknowledgement

This work was financially supported by the China and Germany Postdoctoral Exchange Program 2019 from the Office of China Postdoctoral Council and the Helmholtz Centre (grant number: 20191031). This work contributes to the research performed at CELEST (Center for Electrochemical Energy Storage Ulm-Karlsruhe), and was partially funded by the German Research Foundation (DFG), under the project ID 390874152 (POLiS Cluster of Excellence). The authors are grateful for the editorial support from Leon Geisen and thank all contributors of the PACE3D framework.

References

[1] Zeliang Liu, Mark Fleming, and Wing Kam Liu. Microstructural material database for self-consistent clustering analysis of elastoplastic strain softening materials. *Computer Methods in Applied Mechanics and Engineering*, 330:547 – 577, 2018.

[2] Julian Kochmann, Stephan Wulfinghoff, Stefanie Reese, Jaber Rezaei Mianroodi, and Bob Svendsen. Two-scale FE–FFT- and phase-field-based computational modeling of bulk microstructural evolution and macroscopic material behavior. *Computer Methods in Applied Mechanics and Engineering*, 305:89 – 110, 2016.

[3] Britta Nestler, Harald Garcke, and Björn Stinner. Multicomponent alloy solidification: Phase-field modeling and simulations. *Physical Review E*, 71:041609, 2005.

[4] Anup Basak and Valery I. Levitas. Nanoscale multiphase phase field approach for stress- and temperature-induced martensitic phase transformations with interfacial stresses at finite strains. *Journal of the Mechanics and Physics of Solids*, 113:162 – 196, 2018.

[5] Harald Garcke, Britta Nestler, and Barbara Stoth. On anisotropic order parameter models for multi-phase systems and their sharp interface limits. *Physica D: Nonlinear Phenomena*, 115(1-2):87–108, 1998.

[6] Harald Garcke and Stefan Schaubeck. Existence of weak solutions to the Stefan problem with anisotropic Gibbs-Thomson law. 2011.

[7] Alfred Schmidt. Computation of three dimensional dendrites with finite elements. *Journal of Computational Physics*, 125(2):293–312, 1996.

[8] Milo R. Dorr, Jean Luc Fattebert, Michael E. Wickett, James F. Belak, and Patrice E.A. Turchi. A numerical algorithm for the solution of a phase-field model of polycrystalline materials. *Journal of Computational Physics*, 229(3):626 – 641, 2010.

[9] Yuanzun Sun, Jun Luo, and Jingming Zhu. Phase field study of the microstructure evolution and thermomechanical properties of polycrystalline shape memory alloys: Grain size effect and rate effect. *Computational Materials Science*, 145: 252 – 262, 2018.

[10] Cheikh Cissé and Mohsen Asle Zaeem. A phase-field model for non-isothermal phase transformation and plasticity in polycrystalline yttria-stabilized tetragonal zirconia. *Acta Materialia*, 191:111 – 123, 2020.

[11] Chao Yang, Xitao Wang, Hasnain Mehdi Jafri, Junsheng Wang, and Houbing Huang. Fe-C peritectic solidification of polycrystalline ferrite by phase-field method. *Computational Materials Science*, 178:109626, 2020.

[12] Liesbeth Vanherpe, Nele Moelans, Bart Blanpain, and Stefan Vandewalle. Bounding box algorithm for three-dimensional phase-field simulations of microstructural evolution in polycrystalline materials. *Physical Review E*, 76:056702, 2007.

[13] L. Chen, F. Fan, L. Hong, J. Chen, Y. Z. Ji, S. L. Zhang, T. Zhu, and L. Q. Chen. A phase-field model coupled with large elasto-plastic deformation: Application to lithiated silicon electrodes. *Journal of The Electrochemical Society*, 161(11): F3164–F3172, 2014.

[14] Frank Wendler, Christian Mennerich, and Britta Nestler. A phase-field model for polycrystalline thin film growth. *Journal of Crystal Growth*, 327(1):189 – 201, 2011.

[15] Jingzhi Zhu, Zhe Liu, Venu Vaithyanathan, and Longqing Chen. Linking phase-field model to CALPHAD: application to precipitate shape evolution in Ni-base alloys. *Scripta Materialia*, 46(5):401 – 406, 2002.

[16] Daniel Schneider, Ephraim Schoof, Yunfei Huang, Michael Selzer, and Britta Nestler. Phase-field modeling of crack propagation in multiphase systems. *Computer Methods in Applied Mechanics and Engineering*, 312:186 – 195, 2016.

[17] Kais Ammar, Benoît Appolaire, Georges Cailletaud, and Samuel Forest. Combining phase field approach and homogenization methods for modelling phase transformation in elastoplastic media. *European Journal of Computational Mechanics*, 18(5-6):485–523, 2009.

[18] Valery I. Levitas and James A. Warren. Phase field approach with anisotropic interface energy and interface stresses: Large strain formulation. *Journal of the Mechanics and Physics of Solids*, 91:94 – 125, 2016.

[19] Mahdi Javanbakht and Valery I. Levitas. Phase field simulations of plastic strain-induced phase transformations under high pressure and large shear. *Physical Review B*, 94:214104, 2016.

[20] Fengcang Ma, Siyao Lu, Ping Liu, Wei Li, Xinkuan Liu, Xiaohong Chen, Ke Zhang, Deng Pan, Weijie Lu, and Di Zhang. Microstructure and mechanical properties variation of TiB/Ti matrix composite by thermo-mechanical processing in beta phase field. *Journal of Alloys and Compounds*, 695:1515 – 1522, 2017.

[21] A. Durga, P. Wollants, and N. Moelans. Evaluation of interfacial excess contributions in different phase-field models for elastically inhomogeneous systems. *Modelling and Simulation in Materials Science and Engineering*, 21(5):055018, 2013.

[22] Jörn Mosler, Oleg Shchyglo, and H. Montazer Hojjat. A novel homogenization method for phase field approaches based on partial rank-one relaxation. *Journal of the Mechanics and Physics of Solids*, 68:251–266, 2014.

[23] Daniel Schneider, Oleg Tschukin, Abhik Choudhury, Michael Selzer, Thomas Böhlke, and Britta Nestler. Phase-field elasticity model based on mechanical jump conditions. *Computational Mechanics*, 55(5):887–901, 2015.

[24] Daniel Schneider, Felix Schwab, Ephraim Schoof, Andreas Reiter, Christoph Herrmann, Michael Selzer, Thomas Böhlke, and Britta Nestler. On the stress calculation within phase-field approaches: a model for finite deformations. *Computational Mechanics*, 60(2):203–217, 2017.

[25] Daniel Schneider, Ephraim Schoof, Oleg Tschukin, Andreas Reiter, Christoph Herrmann, Felix Schwab, Michael Selzer, and Britta Nestler. Small strain multiphase-field model accounting for configurational forces and mechanical jump conditions. *Computational Mechanics*, 61(3):277–295, 2018.

[26] Bob Svendsen, Pratheek Shanthraj, and Dierk Raabe. Finite-deformation phase-field chemomechanics for multiphase, multicomponent solids. *Journal of the Mechanics and Physics of Solids*, 112:619–636, 2018.

[27] Oleg Tschukin, Alexander Silberzahn, Michael Selzer, Prince G.K. Amos, Daniel Schneider, and Britta Nestler. Concepts of modeling surface energy anisotropy in phase-field approaches. *Geothermal Energy*, 5(1):19, 2017.

[28] Christoph Herrmann, Ephraim Schoof, Daniel Schneider, Felix Schwab, Andreas Reiter, Michael Selzer, and Britta Nestler. Multiphase-field model of small strain elasto-plasticity according to the mechanical jump conditions. *Computational Mechanics*, 62(6):1399–1412, 2018.

[29] P.G. Kubendran Amos, Ephraim Schoof, Daniel Schneider, and Britta Nestler. Chemo-elastic phase-field simulation of the cooperative growth of mutually-accommodating Widmanstätten plates. *Journal of Alloys and Compounds*, 767: 1141–1154, 2018.

[30] P.G. Kubendran Amos, Ephraim Schoof, Nick Streichan, Daniel Schneider, and Britta Nestler. Phase-field analysis of quenching and partitioning in a polycrystalline Fe-C system under constrained-carbon equilibrium condition. *Computational Materials Science*, 159:281–296, 2019.

[31] Ephraim Schoof, P.G. Kubendran Amos, Daniel Schneider, and Britta Nestler. Influence of stress-free transformation strain on the autocatalytic growth of bainite: A multiphase-field analysis. *Materialia*, 9:100620, 2020.

[32] Michael J. Borden, Thomas J.R. Hughes, Chad M. Landis, Amin Anvari, and Isaac J. Lee. A phase-field formulation for fracture in ductile materials: Finite deformation balance law derivation, plastic degradation, and stress triaxiality effects. *Computer Methods in Applied Mechanics and Engineering*, 312:130 – 166, 2016.

[33] Alphonse Finel, Yann Le Bouar, Anaïs Gaubert, and Umut Salman. Phase field methods: microstructures, mechanical properties and complexity. *Comptes Rendus Physique*, 11(3-4):245–256, 2010.

[34] Kazuyuki Nakahata, Hiroshi Sugahara, Martin Barth, Bernd Köhler, and Frank Schubert. Three dimensional image-based simulation of ultrasonic wave propagation in polycrystalline metal using phase-field modeling. *Ultrasonics*, 67:18 – 29, 2016.

[35] Michael J. Borden, Clemens V. Verhoosel, Michael A. Scott, Thomas J.R. Hughes, and Chad M. Landis. A phase-field description of dynamic brittle fracture. *Computer Methods in Applied Mechanics and Engineering*, 217-220:77 – 95, 2012.

[36] Hervé Henry and Herbert Levine. Dynamic instabilities of fracture under biaxial strain using a phase field model. *Physical Review Letters*, 93(10):105504, 2004.

[37] Hervé Henry. Crack front instabilities under mixed mode loading in three dimensions. *EPL (Europhysics Letters)*, 114(6):66001, 2016.

[38] Hervé Henry. Limitations of the modelling of crack propagating through heterogeneous material using a phase field approach. *Theoretical and Applied Fracture Mechanics*, 104:102384, 2019.

[39] Martin Käser and Michael Dumbser. An arbitrary high-order discontinuous Galerkin method for elastic waves on unstructured meshes — I. The two-dimensional isotropic case with external source terms. *Geophysical Journal International*, 166(2):855–877, 2006.

[40] M. Kronbichler, S. Schoeder, C. Müller, and W. A. Wall. Comparison of implicit and explicit hybridizable discontinuous Galerkin methods for the acoustic wave equation. *International Journal for Numerical Methods in Engineering*, 106(9): 712–739, 2016.

[41] Lucas C. Wilcox, Georg Stadler, Carsten Burstedde, and Omar Ghattas. A high-order discontinuous Galerkin method for wave propagation through coupled elastic–acoustic media. *Journal of Computational Physics*, 229(24):9373 – 9396, 2010.

[42] Fangqiang Hu, M. Yousuff Hussaini, and Patrick Rasetarinera. An analysis of the discontinuous Galerkin method for wave propagation problems. *Journal of Computational Physics*, 151(2):921 – 946, 1999.

[43] Ingo Steinbach and F. Pezzolla. A generalized field method for multiphase transformations using interface fields. *Physica D: Nonlinear Phenomena*, 134(4):385–393, 1999.

[44] Ingo Steinbach and F. Pezzolla. A generalized field method for multiphase transformations using interface fields. *Physica D: Nonlinear Phenomena*, 134(4):385 – 393, 1999.

[45] Randall J LeVeque. *Finite volume methods for hyperbolic problems*. Cambridge University Press, 2002.

[46] Johannes Hötzer, Andreas Reiter, Henrik Hierl, Philipp Steinmetz, Michael Selzer, and Britta Nestler. The parallel multi-physics phase-field framework PACE3D. *Journal of Computational Science*, 26:1 – 12, 2018.

[47] Lili Wang. *Foundations of stress waves*. Elsevier, 2011.

[48] Miroslav Silhavy. *The mechanics and thermodynamics of continuous media*. Springer Science & Business Media, 2013.

[49] Yuancheng Fung. *Foundations of solid mechanics*. Prentice Hall, 1965.